AGU PUBLICATIONS

JGR

Journal of Geophysical Research: Oceans

RESEARCH ARTICLE

10.1002/2016JC011966

Key Points:
- Ice bridge formation and location in Nares Strait control ice distributions and velocities
- Observations during a 4 year period of extended open water between 2007 and 2010 quantify extraordinary sea ice transport
- Between 2003 and 2012, no thinning trend was observed in the Arctic Ocean's multiyear ice passing through Nares Strait

Correspondence to:
P. A. Ryan,
patryan@udel.edu

Citation:
Ryan, P. A. and A. Münchow (2017), Sea ice draft observations in Nares Strait from 2003 to 2012, *J. Geophys. Res. Oceans*, *122*, doi:10.1002/2016JC011966.

Received 13 MAY 2016
Accepted 28 FEB 2017
Accepted article online 4 APR 2017

Sea ice draft observations in Nares Strait from 2003 to 2012

Patricia A. Ryan[1] and Andreas Münchow[1]

[1]School of Marine Science and Policy, College of Earth, Ocean and Environment, University of Delaware, Newark, Delaware, USA

Abstract Time series observation of sea ice draft and velocity from Nares Strait between 2003 and 2012 provides new insights on the statistical properties of sea ice leaving the Arctic for the Atlantic Oceans. Median ice draft is 0.8 m, but it varies annually from 1.5 m in 2007–2008 to 0.5 m in 2008–2009. Probability density distributions of sea ice draft depend on location across the channel with thicker ice near Canada and thinner ice near Greenland. Nevertheless, sea ice motion stops seasonally due to arching land-fast ice that spans the 30–40 km wide channel for up to 190 days per year such as during the 2011–2012 winter. In contrast, the 2006–2010 period exhibits a single ice arch lasting 47 days in April/May 2008. Hence sea ice statistics are weighted by space not by time, using sea ice velocities estimated from colocated velocity observations. Multiyear sea ice with drafts exceeding 5 m constitute between 9% (2003–2004) and 16% (2007–2008) of the observed sea ice. The probability g(D) of this thick, ridged, multiyear ice decays exponentially with draft D at an e-folding scale D_0 of 3.0 $\pm$ 0.2 m. The trend of D_0 with time is statistically indistinguishable from zero. This observation suggests a steady export of multiyear sea ice at decadal time scales. We speculate that our observations document the draining of the last reservoir of thick ice from the Arctic Ocean found to the north of Ellesmere Island and Greenland.

1. Introduction

Arctic sea ice influences global climate. Annual minimum Arctic sea ice extent records were broken in 2005 [*Comiso and Nishio*, 2008], 2007 [*Stroeve et al*., 2008], and again in 2012 [*Laxon et al*., 2013]. Since increased ice-free areas provide a mechanism for positive climate feedback due to reduced albedo, this fueled concerns about an ice-free Arctic. Global climate models predict an ice-free summer before the end of the century [*Kay et al*., 2011; *Meehl et al*., 2012; *Stroeve et al*., 2012; *Vavrus et al*., 2012]. Measuring ice thickness, observationalists provide crucial data to help models better estimate the time it will take for the Arctic to become free of multiyear ice (MYI).

Ice observations are achieved by various methods. These range from drilling through ice to measure its properties directly at a single point [*Johnston*, 2014; *Eicken and Lange*, 1989] to utilizing remotely sensed satellite data which provide estimates of surface properties including sea ice area over vast regions [*Stroeve et al*., 2012]. Along survey tracks, submarine acoustic studies provide ice thickness from below [*Wadhams et al*., 1979; *Blidberg et al*., 1981; *Bourke and Garrett*, 1987], and electromagnetic devices, such as laser altimeters and radars aboard helicopters and fixed wing aircraft measure this value from above [*Haas et al*., 2006; *Farrell et al*., 2012; *Kurtz et al*., 2013]. Others, such as our current study, use discretely moored ice profiling sonars to measure ice thickness from below as time series [*Melling and Riedel*, 1995].

Global-scale satellite data, collected since 1978 demonstrate the rapidly declining Arctic sea ice extent [*Stroeve et al*., 2012]. However, sea ice loss is not restricted to reduction in areal coverage. Observations indicate that the perennial ice cover that remains in the Arctic has also been thinning. This thinning is documented by *Kwok et al*. [2009] using satellite altimeter as well as submarine and moored sonar measurements, by *Shibata et al*. [2013] using satellite microwave sensor data and by *Renner et al*. [2014] using electromagnetic instruments. *Perovich et al*. [2014] and *Kwok and Cunningham* [2010] attribute this thinning to melting of multiyear ice. An increased export of MYI from the Arctic could also lead to thinner perennial Arctic ice cover.

There are two pathways for ice to advect from the Arctic to the North Atlantic Ocean. These are Fram Strait to the east and the Canadian Arctic Archipelago (CAA) to the west of Greenland. Past observations indicate that Fram Strait dominates ice export year-round [*Aagaard and Carmack*, 1989] while the thickest ice may leave the

Arctic via the CAA. For Fram Strait, *Hansen et al.* [2013] analyzed trends in ice advection with moored sonars since 1990. They found no increased advection of ice with thickness above 5 m; in fact, their study revealed that the ice leaving the Arctic via Fram Strait has been thinning. In contrast, *Bourke and Garrett* [1987] found the thickest ice in the Arctic to the north of the CAA from submarine surveys. This finding was confirmed by *Haas et al.* [2006] and *Maslanik et al.* [2007] who found thickening of ice in the region adjacent to the CAA as well as by *Kwok and Cunningham* [2016] who found the area covered by thick ice to have increased. Our study relates to the potential advective flux of this thick Arctic ice to the south. More specifically, we will quantify the change of ice thickness for the 2003 to 2012 period from sensors moored in Nares Strait.

Nares Strait is a 500 km long channel which connects the Arctic Ocean in the north to Baffin Bay in the south between Ellesmere Island and North Greenland (Figure 1). Steep orography channels the atmospheric flow that is generally along the strait from north to south [*Samelson et al.*, 2006]. Winds impact the advection of ice [*Samelson et al.*, 2006] as does the ocean circulation [*Münchow and Melling*, 2008; *Münchow*, 2016]; however, ice motion ceases at our mooring location after an ice arch forms at the southern end of Nares Strait [*Dumont et al.*, 2009] as it does in most years. Thermal imaging, such as Figure 2, reveals these ice arches as strong temperature gradients between thin ice or water (warm) and thicker ice (cold) [*Vincent et al.*, 2008]. Such ice arches form each winter at many locations throughout the CAA [*Smith et al.*, 1990]. After the ice in Nares Strait is blocked, open water or thin ice covers a large area to the south of it as winds continue to advect newly formed ice into Baffin Bay beyond the arch and a latent heat polynya forms [*Melling et al.*, 2001]. This so-called North Water polynya exhibits high biological productivity [*Dunbar and Dunbar*, 1972]. We find evidence suggesting formation of this polynya for at least the last 800 years in viking artifacts dating to the 12th century found at Inuit settlements near Smith Sound [*Schledermann*, 1980]. Using airborne radar, *Dunbar* [1973] documented the formation and spatial extent of this polynya in 1971 and 1972. *Preußer et al.* [2015] analyzed the characteristics of the polynya between 1978 and 2015 with remotely sensed data. *Kwok et al.* [2010] summarizes formation and duration of all Nares Strait ice arches from 1997 to 2007 while Figure 2 shows the spatial surface temperature distribution for a typical day for each year that in this study we report ice thickness and velocity observations.

2. Methods

Starting in 2003, we deployed an array of instruments in Nares Strait (Figure 1). Final recovery of the instruments occurred in August 2012. Figures 1c–1f illustrate the cross-sectional distribution of sensor systems we will use to estimate ice draft for each deployment period. Since ice in the channel is at its lowest level in August, recoveries/redeployments occurred during that month. This results in data gaps of varying lengths during August. We therefore define an ice year as the period from 1 September to 31 July for interannual comparisons. Our study period covers nine ice years.

The instruments deployed included acoustic Doppler current profilers (ADCP) to measure water and ice velocity vectors [*Münchow*, 2016], conductivity, temperature, and depth profilers (CT/D) to measure temperature, salinity, and pressure [*Rabe et al.*, 2010], and ice profiling sonars (IPS) to measure ice drafts [*Melling et al.*, 1995]. Table 1 lists salient details of the instruments used.

2.1. Ice Draft

We estimate ice draft from sonars manufactured by ASL Environmental Sciences Inc. (Model 4) at locations we refer to as KS20 and KS30 (2003–2007), KS25 (2007–2009), and KF30 (2009–2012). Figure 3 shows the mooring design that consists of an anchor below two Teledyne Benthos Inc. 866A acoustic releases, external battery cases, and three subsurface steel floats. The sounder is attached to the top float at nominal depth of 100 m (2003–2009) or 75 m (2009–2012).

The sonar sends acoustic pulses into the water column and measures the time for them to return. Most energy is reflected from the water-ice or, in the absence of ice, the water-air interface. At nominal depth, the narrow angle of the IPS sonar results in a footprint of 7.7 m^2 (2003–2009) or 4.4 m^2 (2009–2012) at the water surface. The measured travel time is converted to a distance, R, to the interface, provided the speed of sound is known. This distance from the sonar to the interface is then converted to an ice draft D provided the vertical location η and beam orientation α of the sonar are known (Figure 4).

The IPS also measures pressure with a Paroscientific Inc. 2200A-101 as well as pitch and roll with an Applied Geomechanics Model 900 unit.

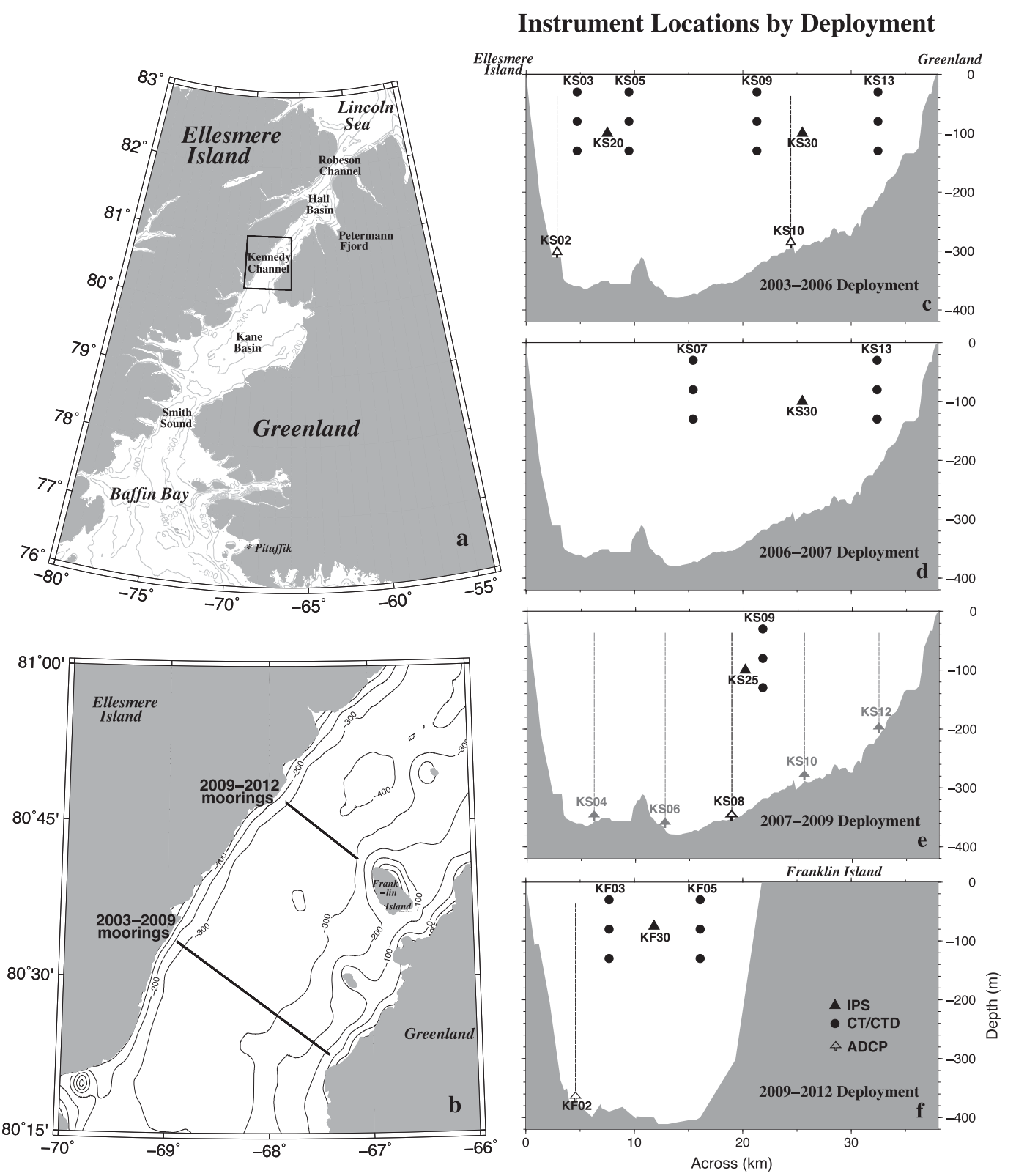

Figure 1. Mooring locations. (a) Map of Nares Strait, (b) inset map showing details for Kennedy Channel section where dark lines spanning the channel indicate the mooring locations. (c)–(f) Cross-section view of strait and moored instruments for each deployment. Note that the 2009–2012 deployment was located north of those in previous years and the IPS instrument was raised to 75 m depth.

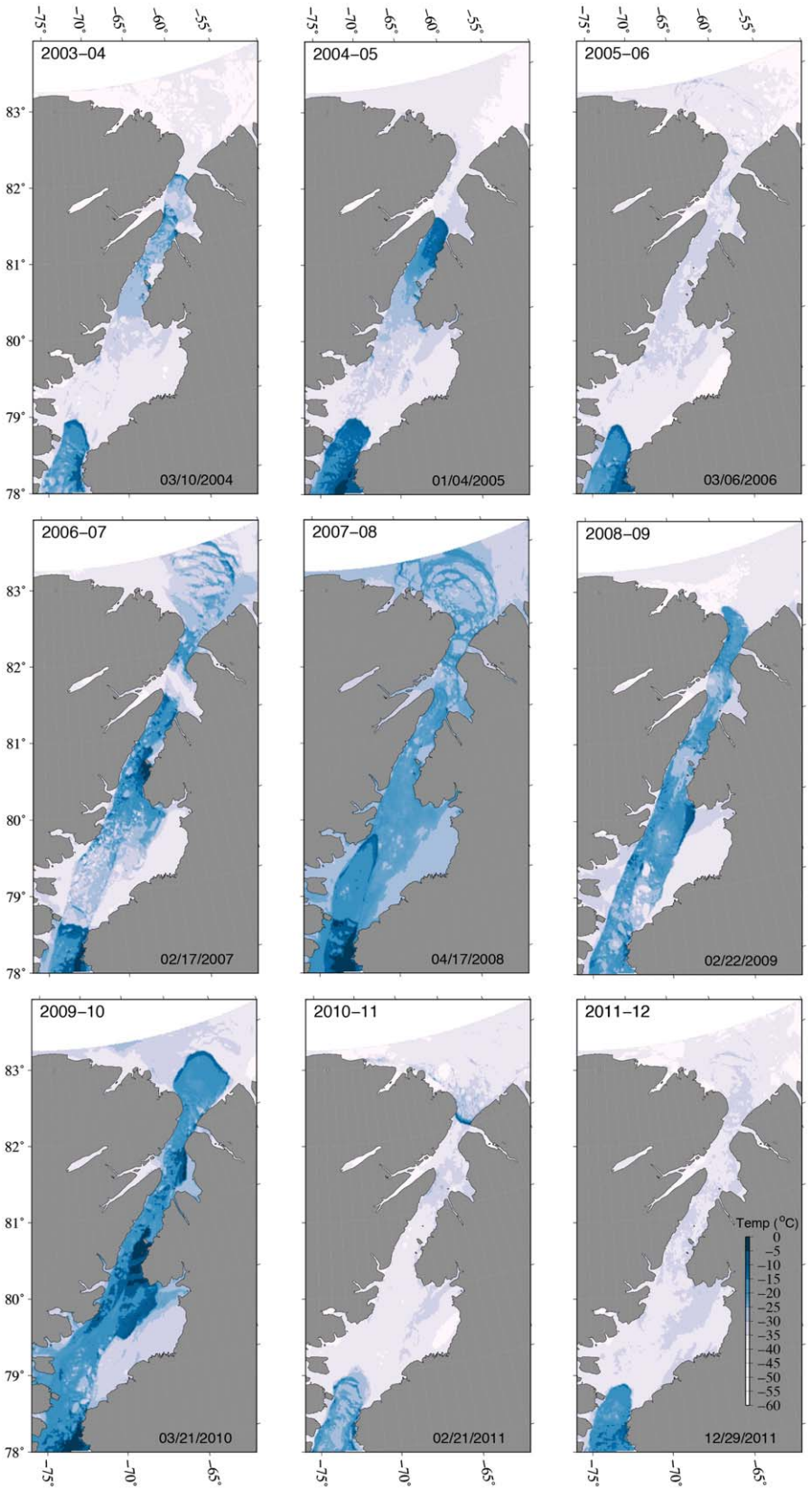

Figure 2. MODIS images of surface temperature in Nares Strait [*Vincent et al.*, 2008]. Ice bridges near 83°N and 79°N appear as cold arches adjacent to a relatively warm zone that lies just south of them with temperature gradients larger than 20°C.

Assuming a constant speed of sound $SS_a = 1440$ m s^{-1}, the IPS records the measured two-way travel time t as range R_{IPS}, i.e.,

$$R_{IPS} = SS_a * t/2 \quad (1)$$

The true range R requires the true speed of sound SS, the derivation of which we describe in the next section. That is, we apply a correction factor

$$\beta = SS/SS_a \quad (2)$$

to find the true range

$$R = \beta R_{IPS} \quad (3)$$

Furthermore, we correct for the measured sensor tilt $\alpha = (\text{tilt}_x{}^2 + \text{tilt}_y{}^2)^{\frac{1}{2}}$, where tilt_x and tilt_y are the pitch and roll measured by the IPS. Hence we determine the vertical distance from the sonar to the reflecting interface R_0 as

$$R_0 = R\cos(\alpha) \quad (4)$$

Finally the draft D of the ice is defined as (Figure 4)

$$D = \eta - R_0 \quad (5)$$

where the water level

$$\eta = (P_l - P_a)/(\rho * g) + d_t \quad (6)$$

and P_l is the pressure measured at the IPS, P_a is atmospheric pressure, ρ is the depth-averaged density of the water column above the instrument, g is the acceleration due to gravity, and $d_t = -0.066$ m is the distance from the transponder to the pressure gauge on the IPS.

Pitch, roll, and pressure were sampled at 60 s intervals. The range, however, was recorded at intervals of 3 s for August through January and 5 s for February through July from 2003 to 2009 while from 2009 to 2012 we chose recording intervals of 2 s for July through January and 3 s for February through June. When deployments exceeded 2 years, ranges were recorded at the longer time interval of said deployment. This variable time step was intended to conserve power and data storage on the premise that ice velocities are higher during mobile versus land-fast ice seasons. We subsampled these data to a uniform 15 (6) second sampling for the 2003–2009 (2009–2012) deployments using linearly interpolated tilt and pressure values to the frequency of the IPS range measurement.

Table 1. Instruments by Deployment

Deployment	2003–2006		2006–2007		2007–2009		2009–2012	
IPS (ice draft)								
Station	KS20	KS30	KS30		KS25		KF30	
Nominal depth	100 m	100 m	100 m		100 m		75 m	
Latitude (°N)	80.53	80.44	80.44		80.48		80.73	
Longitude (°W)	68.65	67.85	67.87		68.14		67.41	
ADCP (ice velocity)								
Station	KS02	KS10	None		KS08		KF02	
Latitude (°N)	80.55	80.44	Deployed		80.47		80.77	
Longitude (°W)	68.87	67.93			68.19		67.73	
Dist. to IPS (km)	4.61	1.45			1.16		7.27	
CT/D (salinity and temperature)								
Station	KS03	KS05	KS09	KS13	KS07	KS13	KS09	KF03	KF05
Latitude (°N)	80.55	80.52	80.46	80.40	80.49	80.39	80.46	80.75	80.70
Longitude (°W)	68.79	68.58	68.06	67.58	68.32	67.59	68.06	67.59	67.22
Dist. to IPS (km)	2.80	2.12	4.28	7.85	16.43	6.90	3.00	4.14	4.27
Nominal Depth	Instrument serial number[type[a]]								
30 m	2918[P]	2919[P]	2921[P]	2923[P]	2920[P]	2921[P]	2921[P]	2921[P]	2917[P]
80 m	2932[P]	2898	2900	2902	2899	2900	2900	2900	2897
130 m	2910	2911	2913	2915	2912	2913	2913	2913	2909

[a] *P* indicates with pressure gauge.

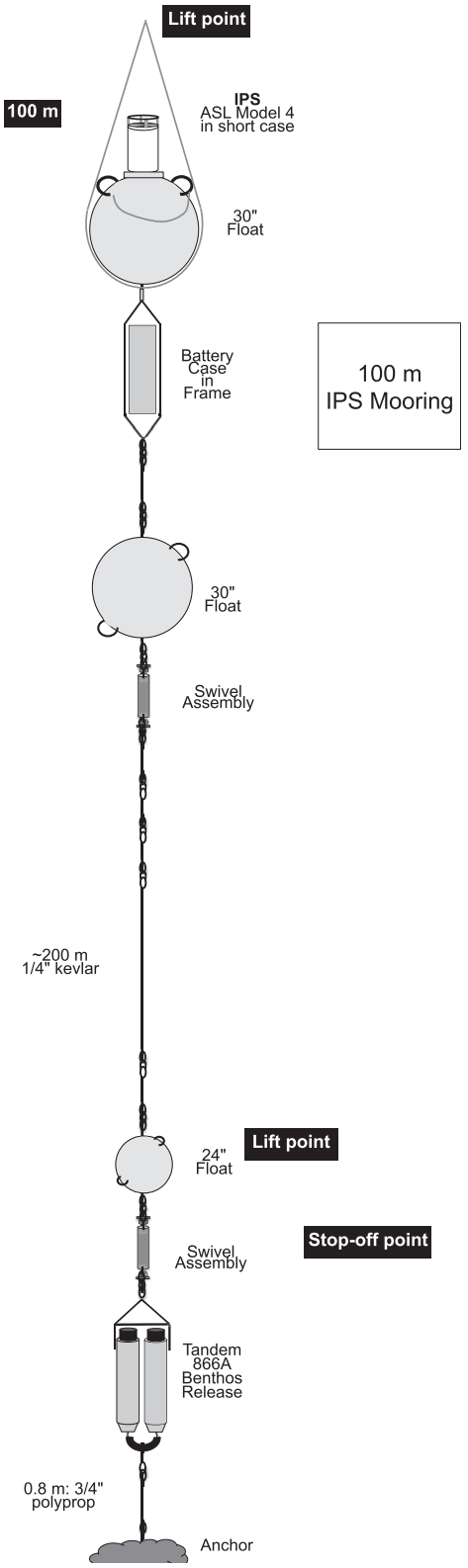

Figure 3. IPS mooring configuration.

In Appendix A, we describe our error budget which shows our ice draft estimates to be accurate to within a standard deviation of 0.1 m or about 0.1% of the range measurement. In order to achieve this accuracy, we used vertical temperature and conductivity profiles from concurrent, nearby mooring locations (Table 1) at daily time scales to estimate the actual speed of sound, SS. We exploit the relatively high occurrence of open water during the month of August to assess these methods. Figure 5 shows the probability distribution of August observations as well as the number of days for which data are available that month. If all observations were open water, we would expect to see a normal or Gaussian distribution centered at the 0 m draft bin. The black outline in the figure shows an idealized Gaussian distribution represented by the formula

$$f(x|\mu,\sigma)=\frac{1}{\sqrt{2\sigma^2\pi}}e^{-\frac{(x-\mu)^2}{2\sigma^2}} \quad (7)$$

where the mean, $\mu=0$ and the standard deviation, $\sigma=0.1$m. Since there is still some ice in the channel, there is additional overlay of ice for the period. As one would expect variability about the mean of zero during periods of open water due to surface waves, we are well within our error estimate. Figure 6 shows draft observations for an entire day, 1 April 2004. This is a representative period during the land-fast ice season when the scale of variability in ice drafts should be limited to the roughness of the ice that is stationary over our instruments. We find that the ice drafts vary between 0.72 and 0.93 m with a mean of 0.88 m and a standard deviation of 0.03 m. This again is well within our error estimate.

Figure 7 shows the bottom topography derived from ice draft observations on 10 August 2005 between 4:00 and 4:45 GMT. During this time, ice of drafts exceeding 10 m passed our instruments after a period of open water. As we measure sea surface during these open water periods, the draft observations are within a few centimeters of zero.

2.2. Ocean Density and Speed of Sound

Equation (2) requires *SS*, the true speed of sound while equation (6) requires ρ, the depth-averaged density. We derive these time-varying parameters from CT/D moorings first described by *Rabe et al.* [2010]. These moorings near the IPS locations contain SBE37sm CT/D sensors at nominal depths of 30, 80, and 130 m. Figures 1c–1f identify the locations of the instruments that recorded data at 15 min intervals. Using the regression analysis described in *Rabe et al.* [2012], we construct time series of density and speed of sound for the water column above the sonar. Appendix A provides further details.

2.3. Atmospheric Forcing

Equation (6) requires P_a, atmospheric pressure, to remove the inverted barometric pressure effect. Since there was no contemporaneous meteorologic data at the mooring

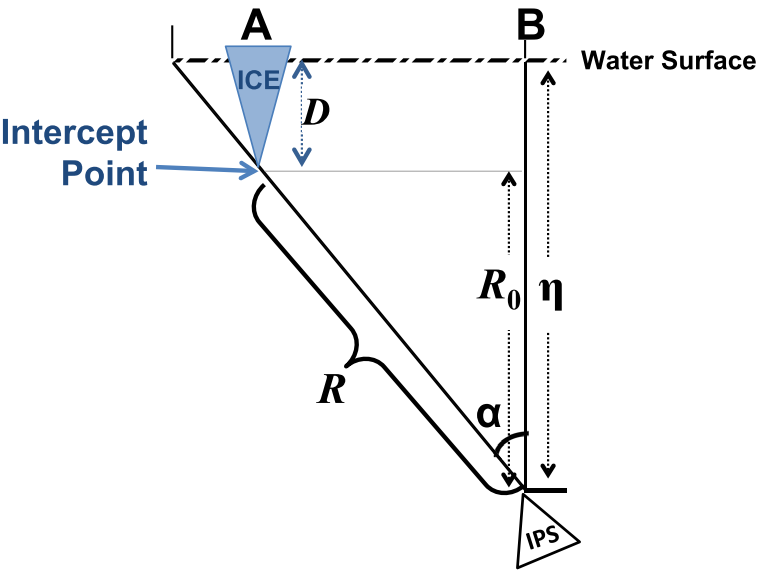

Figure 4. Ice draft cartoon. Ice is located at A, its intercept point is at a distance, *R*, and an angle, α, to the IPS. B is directly above the IPS.

site, output from a regional atmospheric model provided a substitute [*Samelson and Barbour*, 2008] at hourly intervals. Values were interpolated linearly to the sampling interval of IPS range measurements. Appendix B provides further details.

2.4. Quasi-Lagrangian Frame

We measure ice draft and velocity in a spatially fixed or Eulerian frame, however, the ice passing our observing array consists of discrete particles during the mobile season and a fixed surface during the land-fast season. This bimodal character of ice motions provides biased statistics. We therefore present ice draft probability density functions by transforming our Eulerian observations of ice draft D(t) into a quasi-Lagrangian frame D(x(t)), where $x(t) = U_{ice}*t$. We used ADCPs to estimate ice velocity, U_{ice}. We used the Doppler shift from the vertical bin that contains a near-surface maximum of acoustic backscatter to derive this velocity. The root-mean square error is less than 5 cm s^{-1}. The largest errors always occur within 5 km of the Ellesmere Island coast [*Münchow*, 2016]. After introducing our time series data in the next section, we provide all statistical ice properties in this quasi-Lagrangian frame. Ice thickness distributions thus are weighted by ice velocity not time.

3. Time Series Data

3.1. Ice Drafts and Velocity

Our instruments measured ice drafts in Nares Strait for nine years between 2003 and 2012. The daily medians of these measurements are shown in Figure 8 (left). Day-to-day variability ranges from zero to almost ten meters with an annual mean that varies from 0.95 m (2003–2004) to 1.98 m (2006–2007). The largest daily median ice draft in our record is 9.3 m on 16 February 2008.

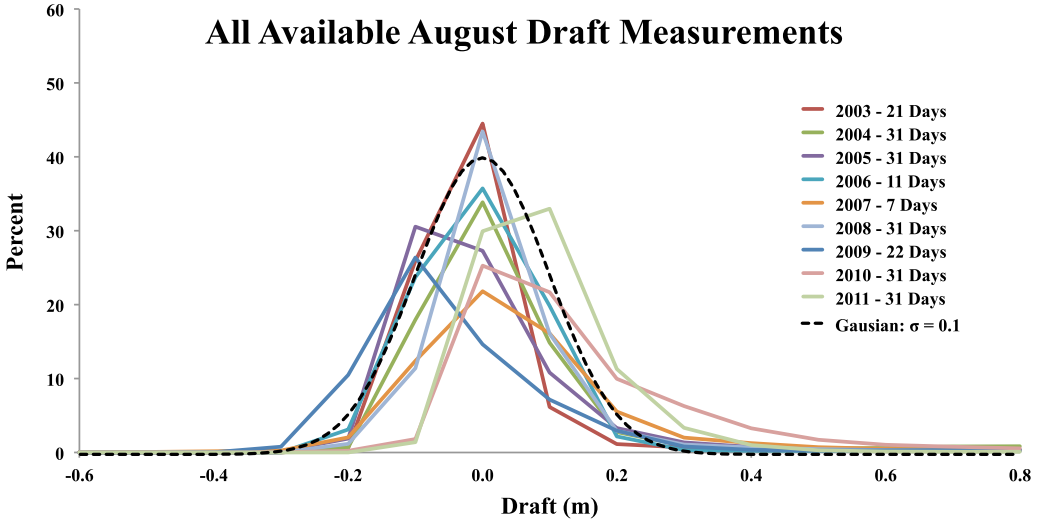

Figure 5. Probability distribution of all observations during the month of August. Dotted black line shows an idealized Gaussian distribution.

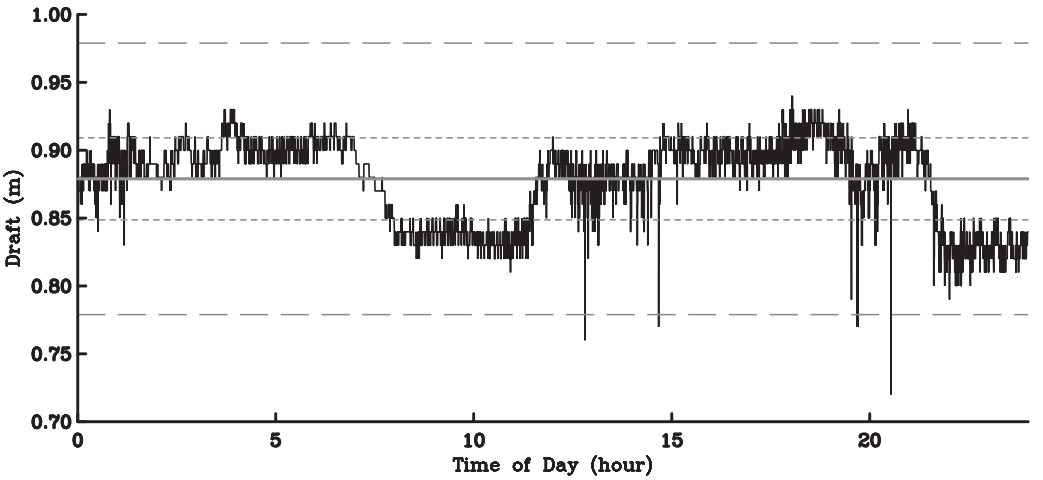

Figure 6. Draft observations on 1 April 2004 (15 s interval). Gray lines show mean (solid), ± one standard deviation of observations (short dashes), and ± our error estimate (long dashes).

Figure 8 (right) shows the along-channel ice velocity, U_{ice}, from an adjacent ADCP mooring. Dominant flow in Nares Strait is from the Arctic Ocean to Baffin Bay with a mean along-channel velocity during our record of 0.25 m s^{-1}. During mobile ice season, this mean rises to 0.35 m s^{-1}.

3.2. Seasonality

Our data describe two distinct ice seasons in the channel. The first is characterized by periods of variable ice draft caused by the rapid advection of thick and ridged MYI that originates in the Arctic Ocean. A second season occurs during periods of little variability when the ice is not moving but grows slowly in place. Gray shading in Figure 8 indicates those times when ice is land-fast.

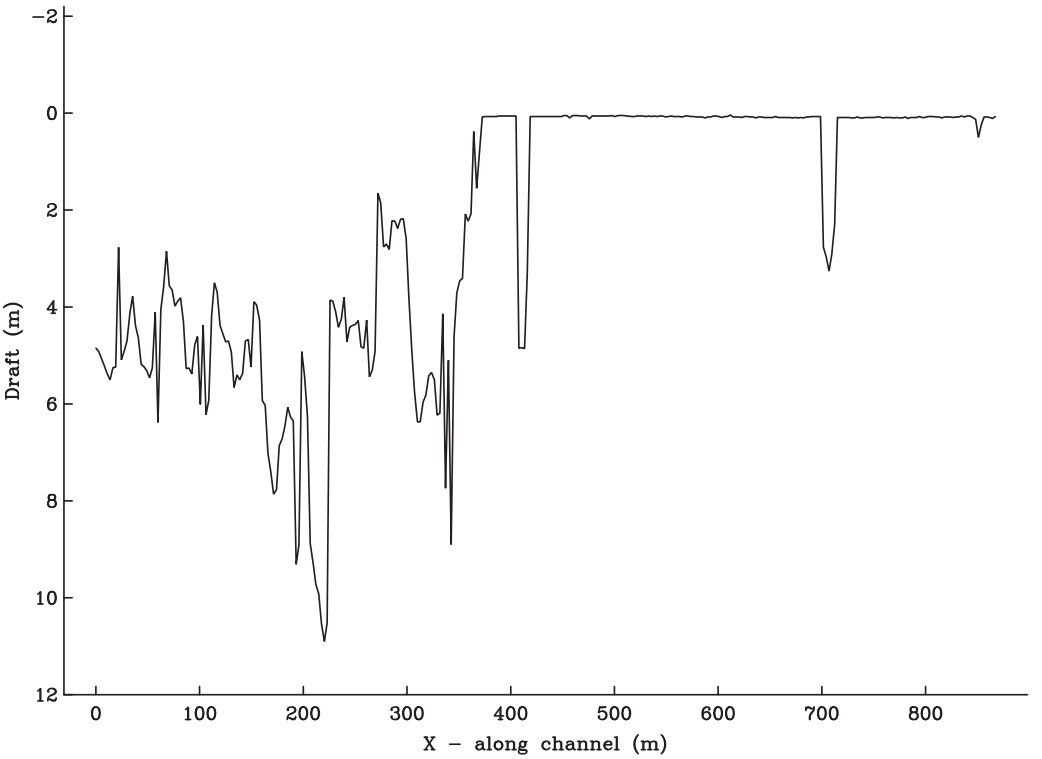

Figure 7. Bottom topography of ice measured on 8 August 2005. Near zero values indicate a period of open water.

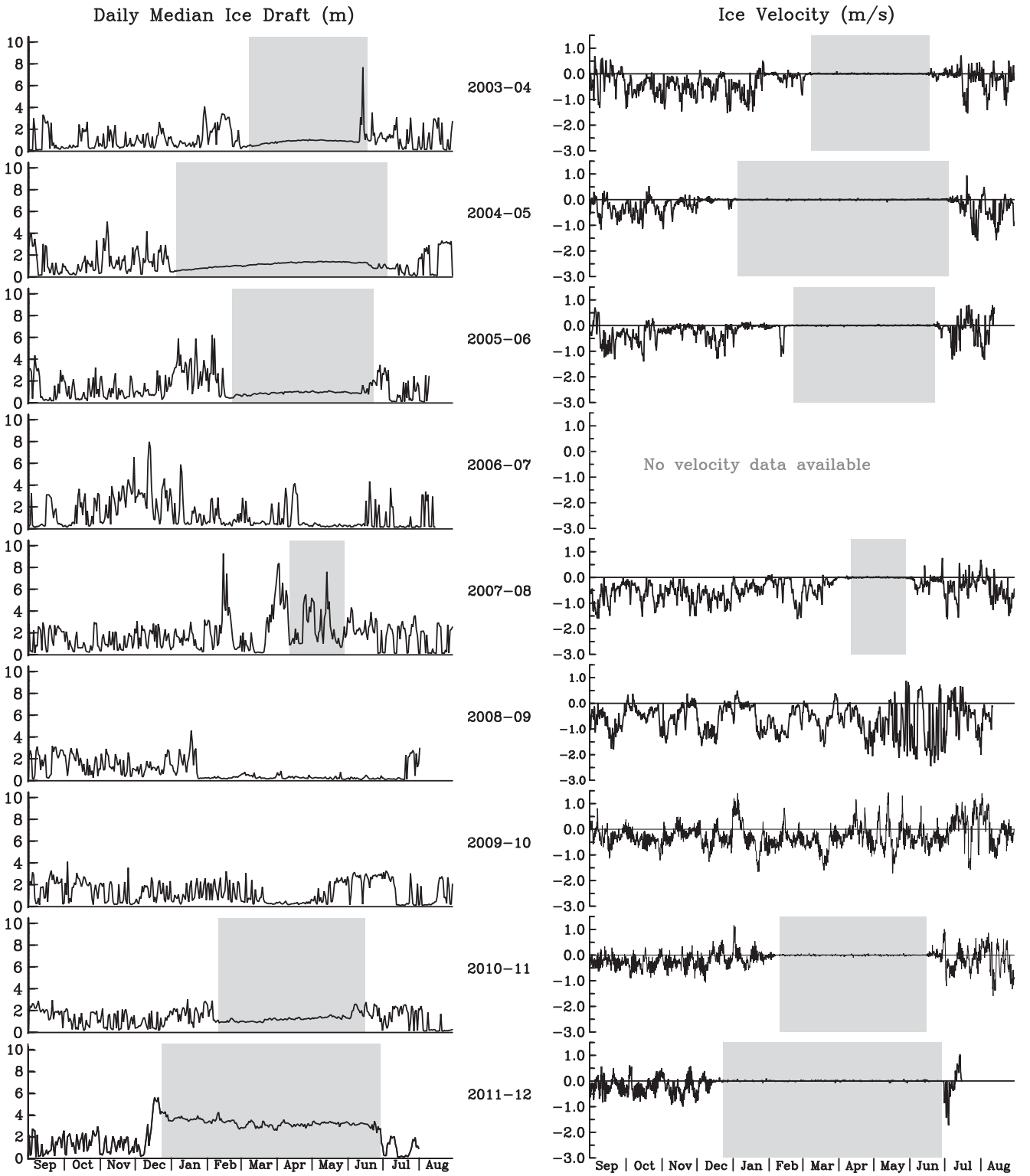

Figure 8. (left column) Daily median ice drafts at KS30 (2003–2007), KS25 (2007–2009), and KF30 (2009–2012). (right column) Along-channel ice velocities nearest these stations. Negative velocities are southward. Gray shading indicates fast-ice periods as defined herein.

Time series of ice velocity allow us to distinguish the mobile from land-fast seasons. We thus define the land-fast season to begin when daily-averaged ice speed remains below 0.025 m s^{-1} for 10 successive days and to end when it exceeds 0.06 m s^{-1} for a single day. For all other times, we define the ice to be mobile.

Table 2. Annual Statistics[a]

Year	Land-Fast Season		North Bridge	South Bridge	Collapse Date	Number of
	Onset Date	Duration (days)	Onset Date	Onset Date		Spatial Bins
2003–2004	8 Mar 2004	102	14 Feb 2004	11 Mar 2004	21 Jul 2004	838,362
2004–2005	4 Jan 2005	182	7 Dec 2004	31 Dec 2004	6 Aug 2005	479,341
2005–2006	22 Feb 2006	122	22 Feb 2006	18 Feb 2006	6 Aug 2006	750,318
2006–2007		0				
2007–2008	12 Apr 2008	47		1 Apr 2008	8 Jun 2008	2,905,780
2008–2009		0	16 Jan 2009		9 Jul 2009	3,021,820
2009–2010		0	17 Mar 2010		15 May 2010	3,527,274
2010–2011	10 Feb 2011	127	16 Jan 2011	30 Jan 2011	30 Jun 2011	1,697,529
2011–2012	23 Dec 2011	190	3 Dec 2011	10 Dec 2011	11 Jul 2012	1,141,927

[a]Ice bridge data for first 6 years are as identified in *Kwok et al.* [2009], except when we find a northern bridge formed in February of 2006 within Nares Strait. The remainder of ice bridge formation dates are estimates to within ± 3 days derived from MODIS imagery.

For each ice year, our definition results in a single continuous land-fast interval, the onset, and duration of which we list in Table 2. The longest land-fast season, persisting 190 days, occurred in 2011–2012. In contrast, ice is mobile year-round in 2006–2007 [*Münchow and Melling*, 2008; *Kwok et al*., 2010], 2008–2009, and 2009–2010.

Generally during the land-fast season, we observe thermodynamic growth in the ice that is held stationary above our moorings; this is evident in a gradually increasing daily median ice draft (Figure 8). There are two exceptions; these occurred during 2007–2008 and 2011–2012. During the first of these, the brief 47 day land-fast season of 2007–2008, we observe high variability in the median ice draft. We postulate that there was ice of at least two distinct categories above our instruments. This median ice draft variability may be attributable to pitch and roll of the moored IPS allowing us to observe each type of ice for a different percent of a given day. This variability is more likely the result of the lack of a northern bridge; this is the only year in which a southern bridge formed but a northern one did not. Without a northern bridge to halt ice motion north of our instruments, small-scale ice motion or dynamic ice processes during this period would cause our instrument to observe different types of ice throughout the land-fast season and our statistical median ice draft to vary accordingly. We intend to address this period in detail in a future paper. The second land-fast ice period where we fail to see evidence of thermodynamic growth in the stationary ice at our mooring location is during the final year of our study. In this instance, we find that the ice above our instruments at the onset of the land-fast season is thicker than in any prior year. We discuss this further in section *Ice bridge control and implications*, below.

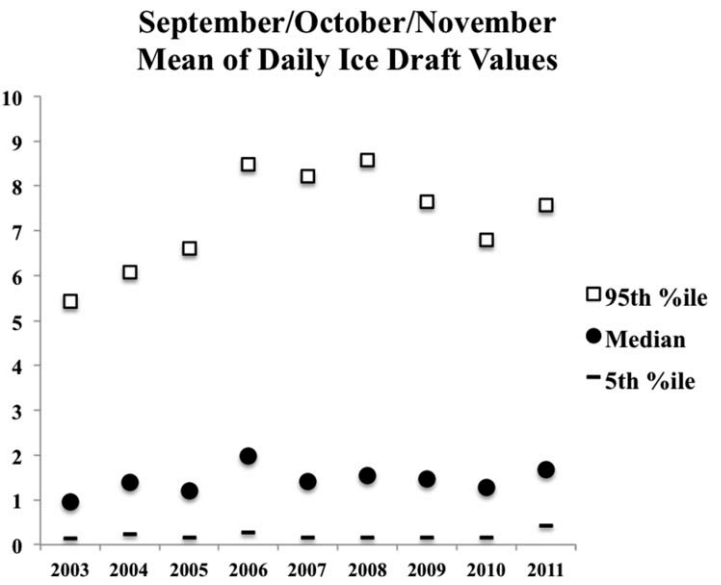

Figure 9. Mean of daily ice draft statistics, 5th percentile, median, and 95th percentile, during the months of September, October, and November for each year.

Focusing on the mobile season, we investigate how ice draft changes for the September, October, and November periods when ice velocities are at their maximum and to the south. Figure 9 shows the 5th, 50th, and 95th percentile ice draft for these three months in each year. For the first eight of our nine deployment years, we found the 5th percentile measurement to vary between 0.13 and 0.27 m but in 2011, this value reached 0.43 m, exceeding twice the average of all

preceding years. The range for the median varies between 0.95 and 1.98 m. The 95th percentile ice ranges from 5.43 m (2003) to 8.57 m (2008), indicating high variability in the thick ice of Arctic origin that is advected through the channel.

4. Ice Draft Distributions

4.1. Definition and Sources

The ice found in Nares Strait varies from nilas that is millimeters thin to glacial ice that can exceed 80 m in thickness [*Münchow et al*., 2014]. The accuracy of our measurements is 0.1 m (Appendix A) and is thus insufficient to distinguish nilas from open water; hence we consider any measured draft less than 0.1 m to be water and exclude it from our distributions. We thus define ice in five categories using the nomenclature of the World Meteorologic Organization for sea ice thickness, "Young Ice" (0.1 m, 0.3 m), "Thin First Year Ice" (0.3 m, 0.7 m), "Medium First Year Ice" (0.7 m, 1.2 m), "Thick First Year Ice" (1.2 m, 2.0 m), and "Old Ice" (2.0 m, ∞). Since our measurements are of draft which accounts for roughly 90 percent of sea ice thickness, we have converted thickness, T, to draft, D, by

$$D = T * 0.9 \tag{8}$$

In terms of origin, young ice is likely to have formed within Nares Strait. We postulate that it entered the channel as seawater, land or glacial runoff, or ice that subsequently melted and refroze locally. In contrast, old ice is formed in the Arctic Ocean where rafting and ridging may occur as the result of forcing by winds and currents [*Thorndike et al*., 1975]. These dynamic processes result in sea ice exceeding the thickness attainable by purely thermodynamic processes. Old Ice enters Nares Strait via the Lincoln Sea in the Arctic Ocean [*Kwok*, 2005]. We know least about the origin of First Year Ice which may have formed locally during the land-fast season or been advected from the north into Nares Strait.

4.2. Near-Decadal Time Scale

Young ice accounts for one quarter of our ice observations. The first year categories comprise 38% in total, with thin ice at 19%, medium ice at 10%, and thick at 9% of all ice. The largest category, however, is old ice which accounts for 37% of our observations.

In order to statistically describe the ice passing through Nares Strait, we construct histograms to approximate probability density distributions. For these we considered only ice greater than 0.1 m in thickness and used the pseudo-Lagrangian method which we describe in Appendix C. Ice draft counts were grouped in 0.1 m bins. Figure 10 shows the cumulative distribution of ice in the channel for the 2003–2012 period, excluding that for the 2006–2007 ice year for which we did not have velocity data. The mode of the distribution is found in the thinnest ice bin, 0.1–0.2 m. Nearly 25% of all ice measured was of draft 0.2 m or less. The median ice draft is 1.0 m.

Figure 11 shows the histogram of the contribution to ice volume which passed our instruments by draft. That is, $D\frac{N_D}{\Sigma N_i D_i}$, where D is the draft of the ice observation, N_i is the number of observations of ice of draft D_i. Each bin spans 0.1 m. We find a bimodal distribution with primary mode at the 2.0–2.1 m bin, thin old ice, and a secondary mode at the 0.2–0.3 m bin, young ice.

4.3. Annual Time Scales

Figure 12 shows the annual ice distributions as histograms for each year. The mode is always found in the thinnest category (0.1–0.2 m) and its magnitude each year is close to 15%, except in the 2008–2009 ice year when it approaches 20%. That year, the ice distribution was characterized by markedly thinner ice that was mobile throughout the year in Nares Strait.

Figure 13 shows the cumulative histogram for each year. The extreme years were 2007–2008 when ice was thick and 2008–2009 when it was thin. The first of these represents a year without any ice bridges and the second, a year with a long-lasting northern ice bridge Figure 2.

Furthermore, Figure 13 suggests that the first 3 years of our 9 year record, identified with black symbols, are dominated by thin ice categories while the last 3 years, marked by white symbols, contain substantial amounts of ice in both thin and medium ice categories. The two extreme years are the transition towards a

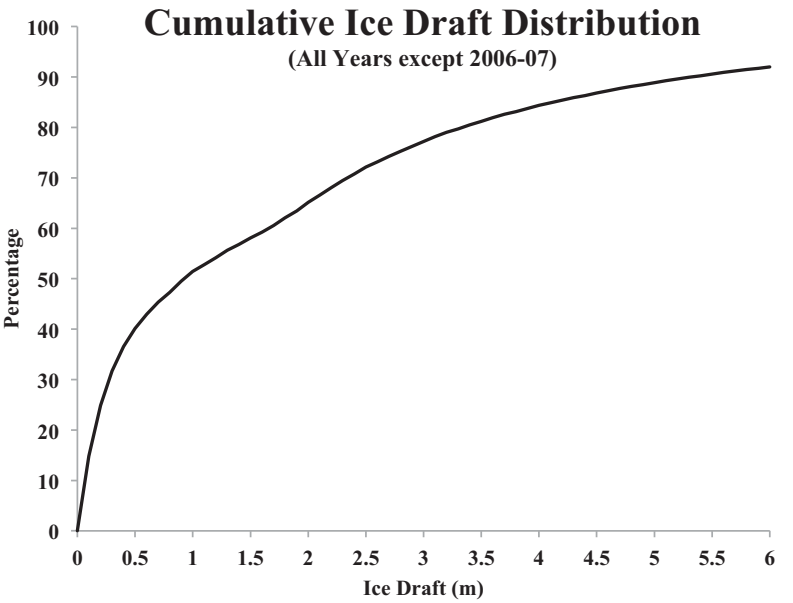

Figure 10. Cumulative percentages of ice observations for all years. Distribution is adjusted for ice velocities and therefore 2006–2007 ice year is excluded.

thicker ice regime. We speculate that the presence, duration, and location of ice arches (Table 2) control ice thickness distributions for a given ice year.

Figure 14 shows histograms of the contribution to ice volume which passed our instruments by draft for each year. Each bin spans 0.1 m; however, for ease of reading we will discuss bins by their midpoint. We find bimodal distributions with primary mode for the first 3 years in the 0.95 m bin and a secondary mode at 3.15 m. In 2007–2008, the primary mode is found in the 2.05 m bin and the secondary is at 0.25 m, whereas the period 2008–2009, dominated by thin ice, has a primary mode in the 0.25 m bin with a secondary at 2.05 m. The remaining years are characterized by a primary mode in the thicker 2.05 or 2.55 m bin and the secondary mode in the 0.25 m bin. These statistical properties of the distributions are shown in the inset of Figure 14.

4.4. Across-Channel Variability

The flow of water in Nares Strait varies across the channel. *Rabe et al*. [2012] identified a jet below 30 m depth of intense along-channel flow in the water column close to the coast of Ellesmere Island. Remote

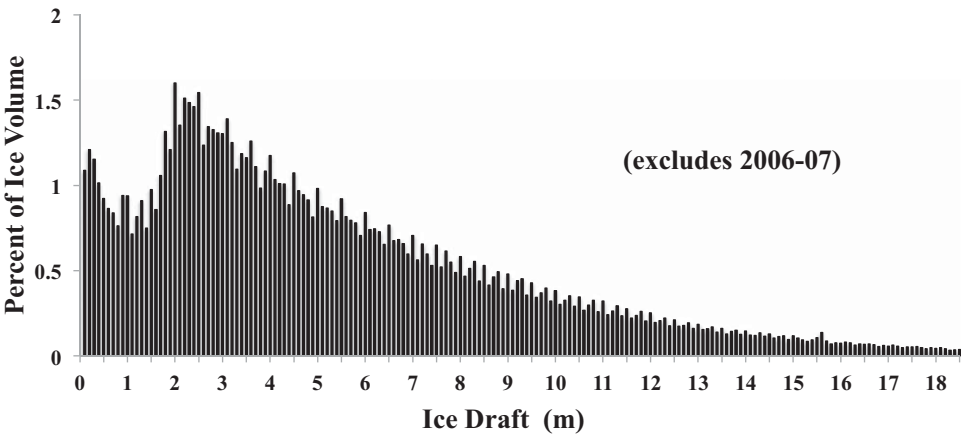

Figure 11. Ice volume fraction by draft. Each bin spans 0.1 m and the percent shown is the relative volume of ice. Distribution is adjusted for ice velocities and therefore 2006–2007 ice year is excluded.

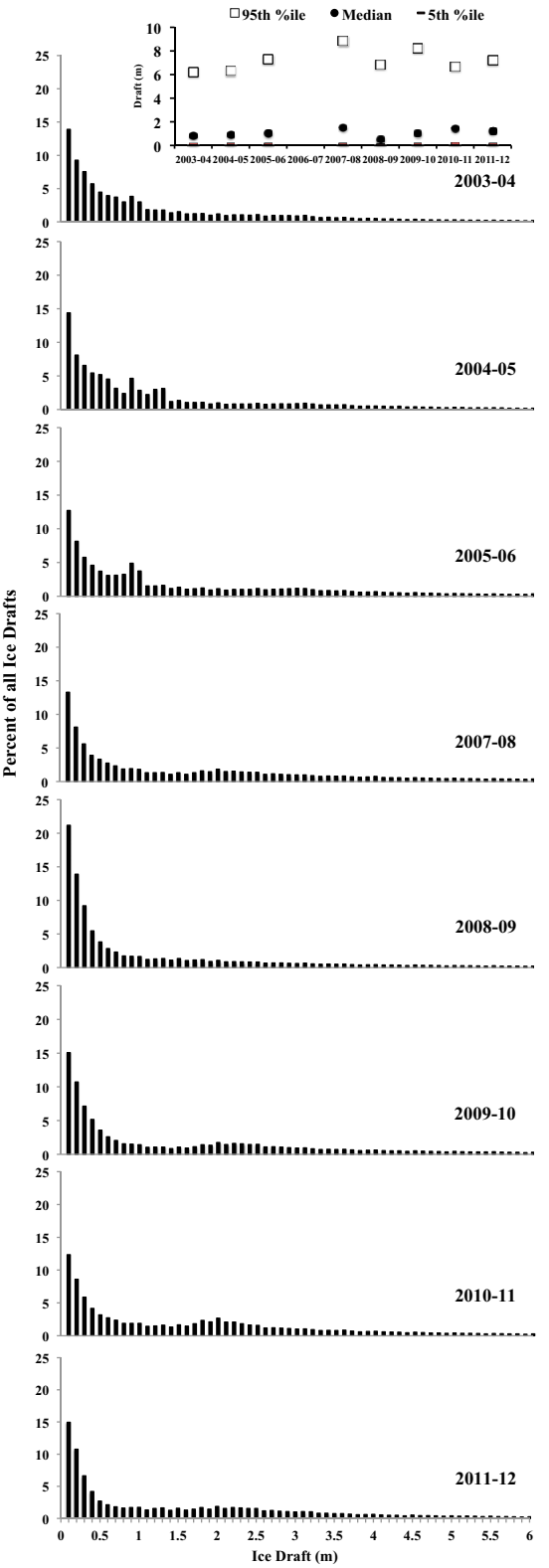

Figure 12. Annual probability distribution of ice drafts as a percent of all ice by year (adjusted for velocity). Bins are in 0.1 m increments. Inset to upper right provides statistics of the annual distributions. Note that 2006–2007 ice year is not included as velocity data are unavailable.

sensing studies suggest that thick ice moves southward along the strait with a preference to the Ellesmere Island coast. This is consistent with a buoyancy-driven geostrophic flow. The across-channel variability of ice flow, however, has not been quantified. During 3 years of our study, 2003–2006, we measured ice draft and velocities at two locations, KS20 and KS30. These stations are separated by 18 km, with KS20 located 7.5 km from the coast of Ellesmere Island. Figure 15 shows the probability density function of ice drafts in 0.1 m bins comparing that of KS20 to KS30; inset graph provides the 5th, 50th, and 95th percentiles for each of these distributions. We find that the ice is generally thicker at KS20. This agrees with remote sensing imagery. During 2003–2006, we found the average ice velocity to be 0.06 m s^{-1} at KS20 while it was 0.17 m s^{-1} at KS30 (Figure 16).

Although we only have ice draft data at one location between 2007 and 2009, we measured surface velocities at five locations across Nares Strait (Figure 1e) identifies these locations at KS02, KS04, KS08, KS10, and KS12. *Münchow* [2016] utilized these data to show that along-channel ice velocities vary across the channel. During this period, *Münchow* [2016] also found that the velocity near Ellesmere Island at the KS20 location was somewhat lower than in the center of the channel at KS30.

4.5. Thick Ice

Wadhams [1981] found the distribution of thick ice in the Arctic Basin to be nearly exponential, e.g.,

$$g(D) = g_0\, e^{D/D_0} \tag{9}$$

Following *Thorndike* [2000], we derive the probability distribution for thick ice, $g(D)$, that has an e-folding decay scale, D_0, and a probability at zero draft, g_0. We estimate D_0 and g_0 by minimizing the least square error between the model $g(D)$ and our data (Figure 17). Episodically glacial ice is present in Nares Strait. Specifically, we see evidence of an ice island from Petermann Fjord passing our instruments on 22 September, 2010, after a large calving event [*Münchow et al.*, 2014]. We found that prior to this calving, less than 2% of all ice exceeded 18.5 m in any ice year and chose this value as an upper limit in our study.

We utilize $g(D)$ to evaluate the change of thick ice between 2003 and 2012. The inset of Figure

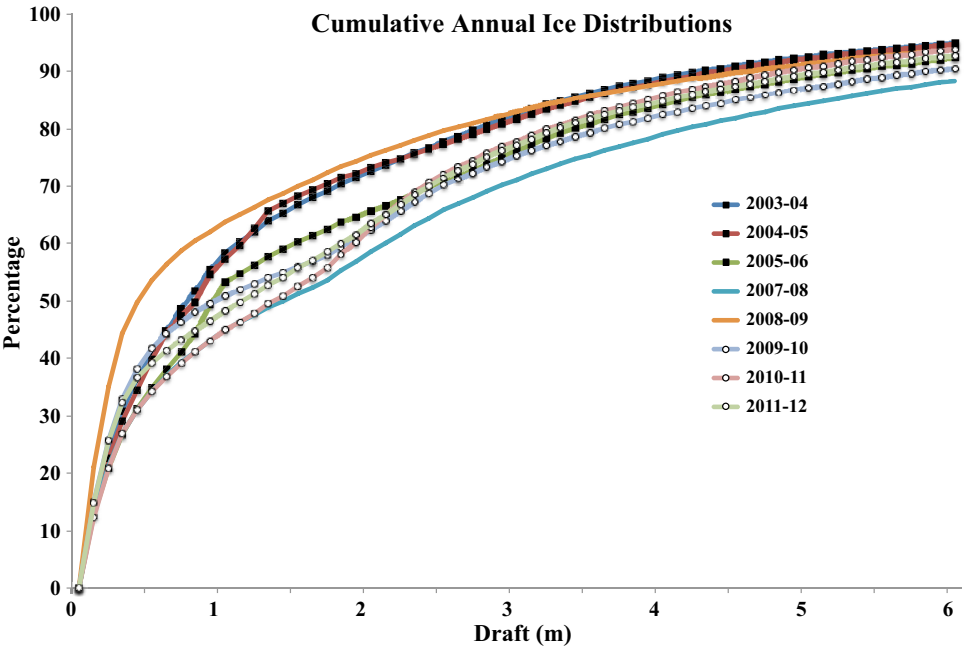

Figure 13. Cumulative probability distribution of ice drafts shown in Figure 12. Black symbols are associated with early record and white symbols with later period.

17 shows that the *e*-folding scale $D_0(t)$ ranges from 2.4 m in 2010–2011 to 3.3 m in 2009–2010 with an average of 3.0 $\pm$0.2 m. Where a larger *e*-folding scale indicates a thicker ice distribution. For comparison, *Thorndike* [2000] reports values of 1.9 m and 2.6 m for studies conducted in the Arctic Ocean in 1993 and 1996, respectively.

The temporal trend of $D_0(t)$ in Nares Strait is -0.03 ± 0.08 m yr^{-1} which is statistically indistinguishable from zero. Thus we find variability to ice distributions over the period rather than a thinning or thickening trend in thick ice in Nares Strait from 2003 to 2012. In contrast, thick ice in Fram Strait was observed to become thinner [*Hansen et al.*, 2013].

5. Ice Bridge Control and Implications

Seasonal ice bridges span Nares Strait and have the ability to block ice flow for many months at a time (Figures 2 and 8). The ice bridges control ice flow and influence ice thickness distributions. When a bridge forms at the southern location, the ice flow is halted throughout the strait. Thermodynamic ice growth is observed in thin and medium ice during these land-fast seasons.

5.1. Impacts of Land-Fast Seasons

Ice is always mobile in Nares Strait from August to November when ice of all thicknesses pass over our moored array. In most years at some time between December and February, the ice stops moving when a southern ice arch between Canada and Greenland shuts down all advection of ice. Our observations indicate that this event coincides with a prolonged period of slow and uniform increase of the ice draft at a time when air temperatures in Nares Strait are generally below -10°C [*Samelson and Barbour*, 2008]. Figure 18 shows atmospheric temperatures produced by the same model [*Samelson and Barbour*, 2008] we used to derive atmospheric pressure over our instruments from 2003 through 2009. In the same figure, we show daily average water temperature observations at a nominal 30 m depth nearest the central channel IPS location.

This growth of stationary ice is evident in the daily median ice drafts during the land-fast ice seasons (Figure 8). In some years, when the ice is less than 2 m thick, we see a gradual increase in thickness of the ice that is immobile above our instruments. Toward the end of the land-fast season, ice thickness begins to fluctuate as the bridge collapses.

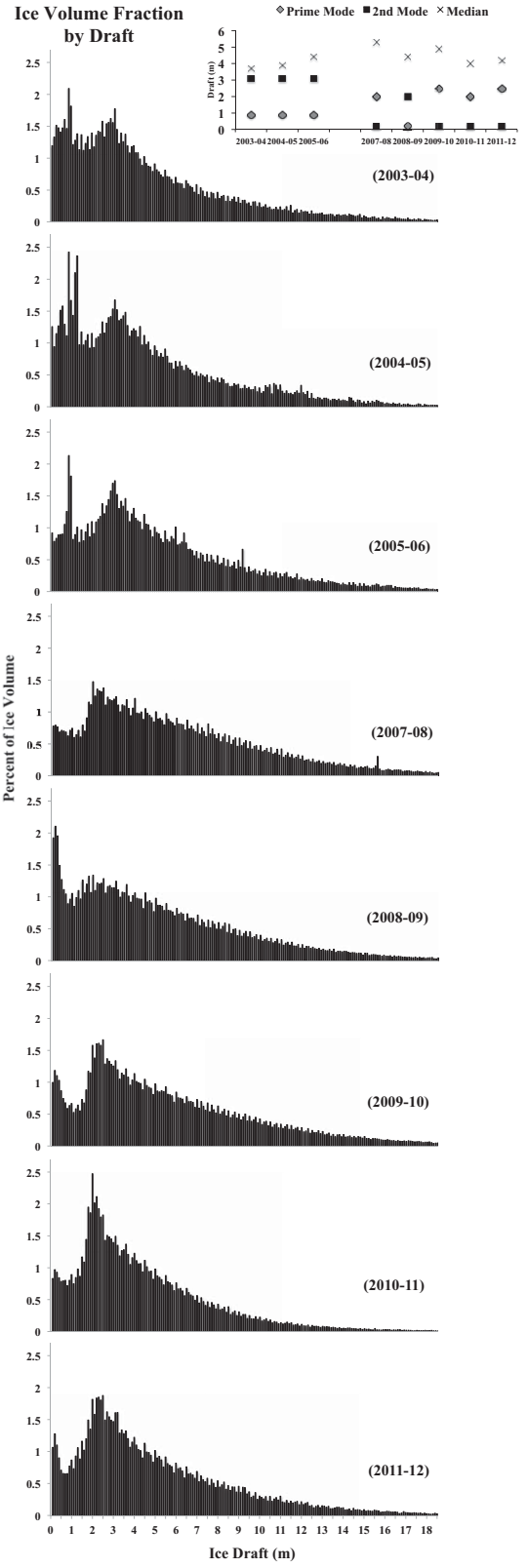

Figure 14. Annual ice volume fraction by draft. Each bin spans 0.1 m and the percent shown is the relative volume of ice. Distribution is adjusted for ice velocities. Inset at top is a chart of the modes and the median of each distribution.

In the final year of our study, we do not see growth in in the ice observed during the land-fast season. This year, the ice trapped above our instruments at the onset of the land-fast season is ∼4 m thick. We explain the lack of ice growth in this year with the analytical results of *Maykut and Untersteiner* [1971]. They predict that ice stops growing when the heat flux into the ice from the ocean equals the heat flux out of it into the air. The heat flux across the ice-ocean and ice-air interfaces depend on factors such as the wind speed, snow cover, thermal conductivity of sea ice, ocean mixed layer turbulence, etc. [*Hibler*, 1979], but ice in the Arctic Ocean generally stops growing thermodynamically when it reaches a thickness of about 3 m. Consistent with this prediction, we find no ice growth in the stationary ice above our instruments during the 2011–2012 land-fast season, because the initial ice is more than 4 m thick. The thick ice insulates a warm ocean from the cold atmosphere above and thus thwarts the transfer of heat from the ocean to the atmosphere necessary to freeze sea water.

The southern ice arch in Nares Strait generally collapses by the last week of July [*Canadian Ice Service*, 2011]. As ice starts moving again, median drafts fluctuate at daily time scales, because a variety of ice floes now pass over our sensors.

5.2. Free-Flow Ice Years

Our 2003–2012 observational period covers 3 years when no southern ice arch forms and sea ice advects over our array throughout the year (Figure 2). These free-flow years are 2006–2007, 2008–2009, and 2009–2010 when daily median ice drafts initially fluctuated within the typical range between 0 and 10 m until they stabilized below 2 m for 1.5–6 months without any thick ice present. We explain this shutdown of the transport of old ice with the formation of an ice arch to the north of our mooring array. Remote sensing indicates a northern ice bridge in 2008–2009 and 2009–2010, but not in 2006–2007. In none of these free-flow years did we see evidence of the period of thermodynamic growth that was observed during land-fast ice seasons of other years. With no southern bridge to block ice transport out of the channel, residence time of a floe was too short to detect local sea ice growth.

During free-flow ice years, ice advection through the channel is continuous and newly formed thin ice and medium ice is swiftly advected. We find

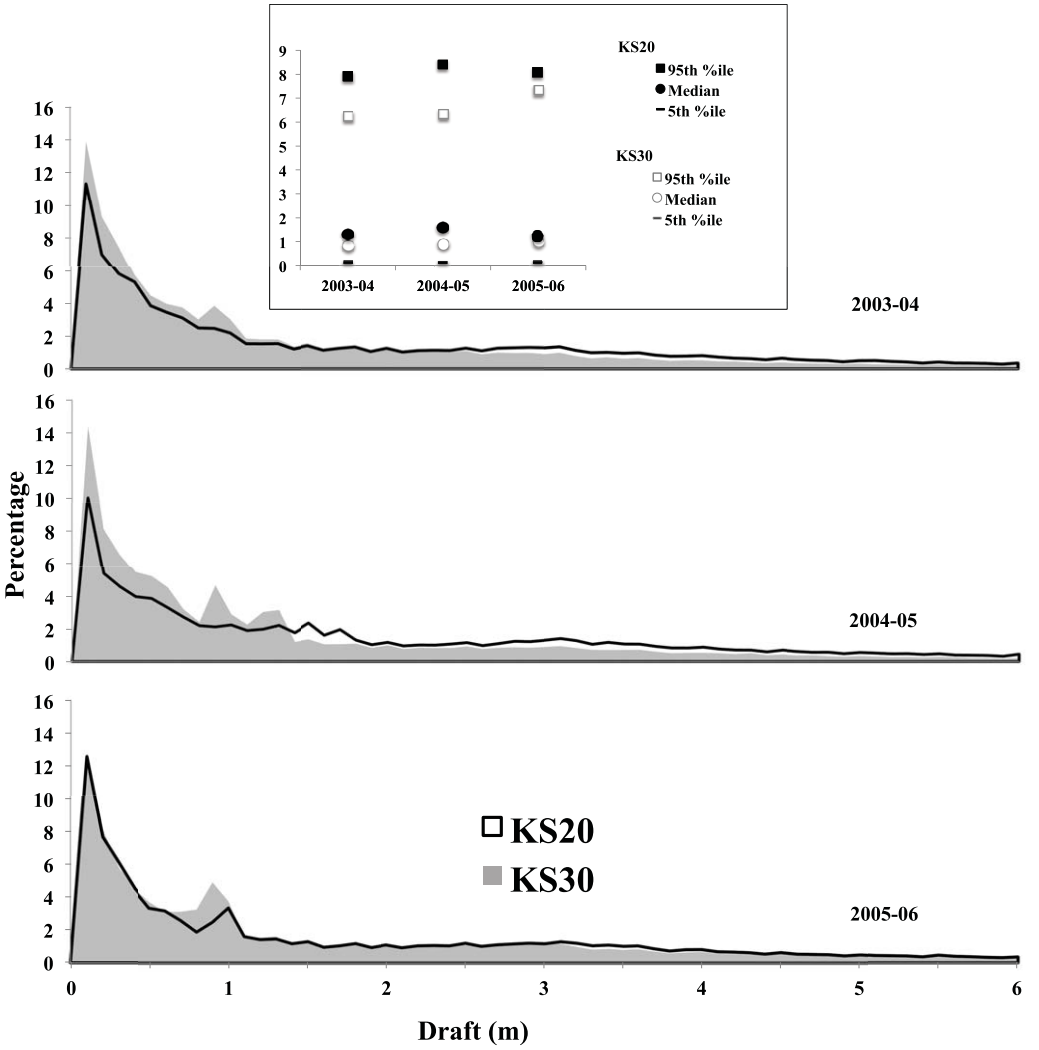

Figure 15. Probability distribution of ice at KS20 (black line) compared to ice at KS30 (gray shade). Inset chart shows 5th, 50th, and 95th percentile for each of these distributions.

these years, 2008–2009 and 2009–2010, to be characterized by lower median ice drafts. As these were the 2 years with only a northern ice bridge, advection of old ice into Nares Strait through the Lincoln Sea was prohibited for nearly 5 months in the former and 2 months in the latter, thus restricting the ice observation to young and first year ice. In 2008–2009, there is a long period, beginning in late January and lasting through mid-July when the daily median draft did not exceed 0.75 m, this coincides with the timing of the northern bridge. During this period, we observed the largest southward ice velocities in our record, exceeding 2 m s^{-1} (Figure 8). This intensified flow, which rapidly flushes ice through the channel, frees the surface for the formation of new ice. We suggest that the enhanced production and advection of local ice within Nares Strait during this period would be equivalent to an evaporative process in the channel. Since the salt rejection rate decreases with ice age, when residence time in the channel is brief, enhanced salinization of the water of Nares Strait would be expected when only a northern bridge forms.

Model studies by *Dumont et al.* [2009] found that formation of an ice bridge in such a channel is dependent on a supply of ice of sufficient thickness. They also found an upper boundary for ice thickness, above which the ice is too resistant to form an arch. Either a shortage of thick ice or an overabundance of very thick ice may be related to ice flow patterns north of the Lincoln Sea. *Kwok* [2015] found that the oscillating

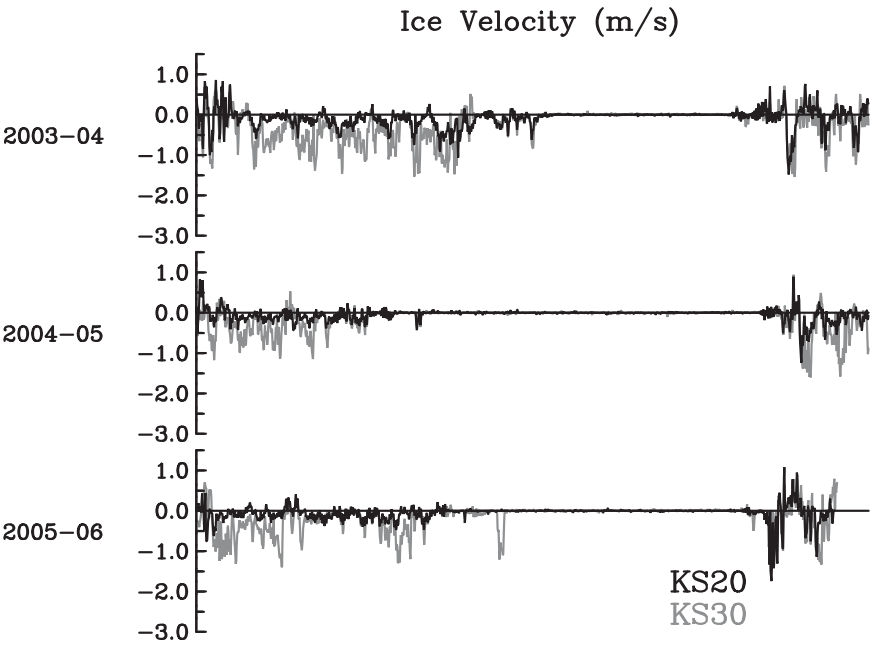

Figure 16. Ice velocity at KS20 (black) compared to KS30 (gray).

convergent/divergent conditions in the Arctic Ocean were related to the longstanding patterns of oscillation known as the North Atlantic Oscillation and Arctic Oscillation. He defines convergent periods, as those during which ice flow tends to be toward shore in the central CAA. He derived an index to quantify convergence in the Arctic Basin. By this measure, our free-flow ice years coincide with a prolonged period of intensified convergence between November 2006 and January 2009.

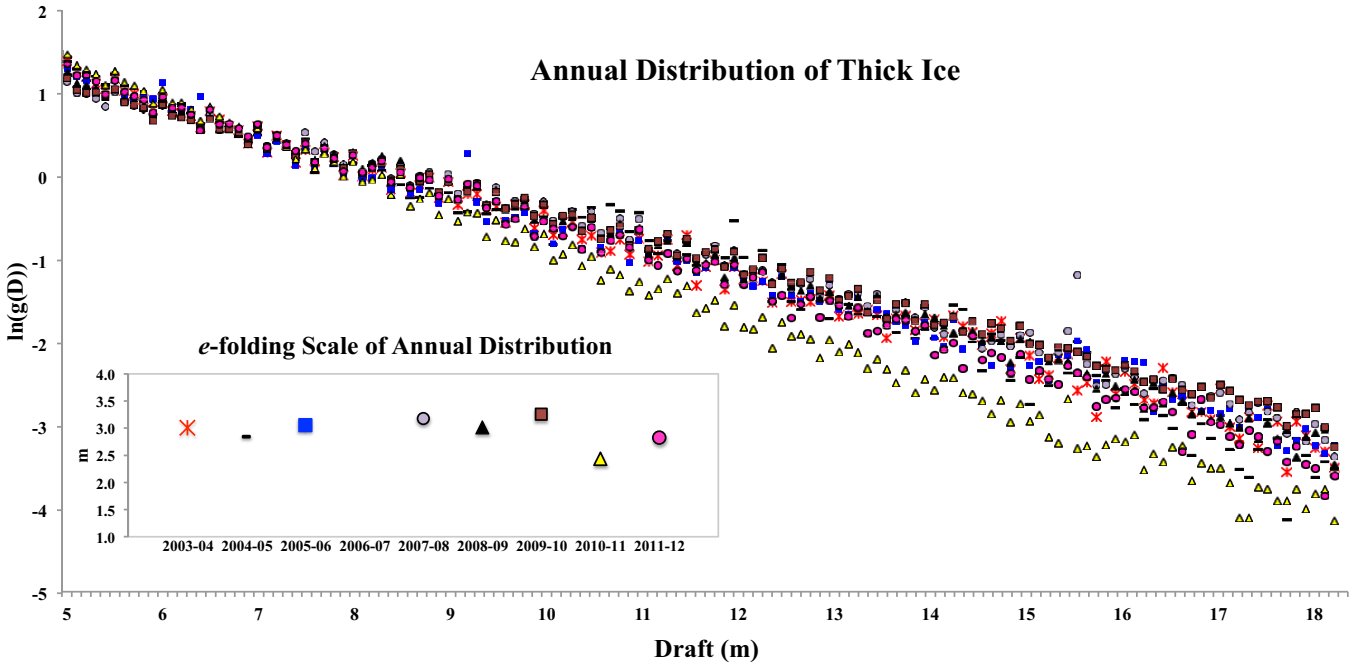

Figure 17. Distribution of thick ice on a log-linear graph (large graph). Symbols indicate observation year. Inset graph shows the *e*-folding scale of the analytic function for each year's ice distribution.

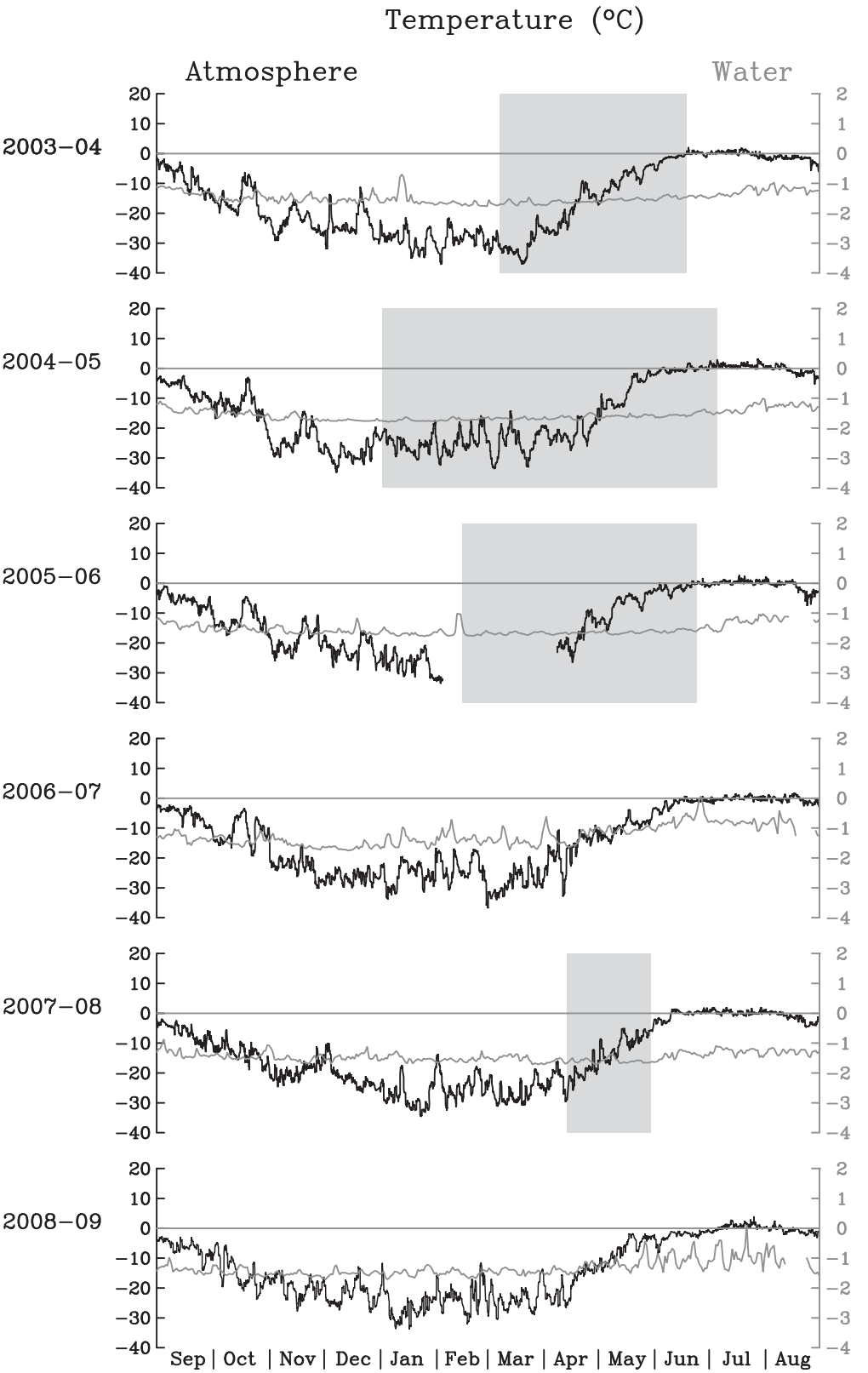

Figure 18. Atmospheric temperatures (black) at our central channel mooring site as derived from regional model. Daily average water temperature observations (gray) from CT instruments at 30 m nominal depth. Gray shading indicates land-fast ice seasons.

6. Discussion and Conclusions

Thick multiyear sea ice exits the Arctic Ocean via Fram and Nares Straits to the east and west of Greenland, respectively. While the sea ice advected southward in the East Greenland Current has been well-documented with both in situ [*Hansen et al*., 2013] and airborne sensors [*Renner et al*., 2014], the ice characteristics in Nares Strait are largely unknown. For example, *Kwok et al*. [2010] estimates ice flux from remote sensing. They assume First Year (FY) ice to be 1.5 m thick and estimate MultiYear (MY) ice thickness from two crude snapshots per year. Our observations from 2003 through 2012 at 15 s intervals paint a more complete picture on the type, quantity, and probability distribution of the sea ice in Nares Strait that does not always agree with prior assumptions. Our unique data contain substantial variability both from year to year and across Nares Strait but it also describes, we speculate, two distinct patterns with and without year-round sea ice mobility related to ice arch formation and decay.

We measured ice draft across a 38 km wide section with two instruments for 3 years. The locations bracket the eastern and western edge of a strong baroclinic circulation where mean ocean speeds and ice velocities exceed 0.3 and 1.0 m s^{-1}, respectively [*Münchow*, 2016]. The median ice draft is 1.33 m off Canada in the west while it is 0.88 m off Greenland in the east. Sea ice off Canada is 50% thicker than it is off Greenland which is consistent with an Ekman-layer response of the surface ocean and sea ice to local winds from the north. This wind direction indeed dominates the atmospheric circulation [*Samelson et al*., 2006]. Furthermore, this Ekman-like response would move sea ice from Greenland toward Canada causing a surface divergence with upwelling off Greenland and surface convergence with downwelling off Canada.

We also find substantial interannual variability in across-channel ice draft differences that are partially explained by different winds in different years. For example, median ice draft off Canada is 52%, 75%, and 23% larger than off Greenland in 2003–2004, 2004–2005, and 2005–2006 while the mean along-channel winds for the same periods are 4.9, 4.3, and 3.9 m s^{-1} from north to south. The correspondence of local along-channel winds and across-channel ice draft differences is not perfect, however, as other processes impact ice draft. One such process is the duration of ice arches that turn mobile FY and MY ice into a fixed frozen matrix of land-fast ice such as shown in Figure 2. These ice arches act as dams to shut down all upstream ice motion while the ocean beneath moves largely unimpeded. Large polynyas result [*Dumont et al*., 2009] and our 9 year record covers a range of ice arch configurations.

No ice arch formed in 2006–2007 and thick MY sea ice moved unimpeded through Nares Strait [*Kwok et al*., 2010]. Median ice draft then was at its maximum during our 9 year observational period reaching 1.98 m while the 95th percentile draft exceeded more than 8 m. We conclude that the absence of any ice arch resulted in the southward export of a record volume of sea ice to exit the Arctic Ocean via Nares Strait. The following year the Arctic Ocean had a historical summer minimum in sea ice cover *Stroeve et al*. [2008] that, we conclude, was partially caused by the large export of thick MY ice from the Lincoln Sea during the previous winter. *Maslanik et al*. [2011] offer a range of additional processes all contributing to the thinning of Arctic Sea ice over the last decade that they refer to as "...evidence of a regional tipping point." We here add enhanced MY ice export through Nares Strait to this list. We furthermore conclude that the ice flux estimate of *Kwok et al*. [2010] is likely biased low, because their assumed ice thickness is smaller than our direct in situ observations.

Apart from a brief two month period, only a northern ice arch formed from 2007 through 2010 and our moorings were located downstream of this Lincoln Sea ice arch. Sea ice during this period was mobile all year, however, it was limited to thin FY that in 2009 was flushed out of Nares Strait rapidly to result in an anomalous open water season that began in May and lasted until July after the ice arch broke. Thick MY ice then streamed southward to our mooring location like a breaking dam. Hence ice navigation was more challenging during the summer in August with air temperatures of 0°C as compared to the winter in May when air temperatures are still at −10°C. We conclude that navigation of Nares Strait is impacted by location and stability of ice arches rather than the predictable seasonal variation of solar radiation and air temperature.

It is tempting to speculate, that this 4 year period of extended open water and thin sea ice in Nares Strait contributed to enhanced wind forcing and mixing to impact the stability of the floating ice shelf of Petermann Gletscher [*Shroyer et al*., 2017]. This large outlet glacier discharges glacier ice and freshwater into Nares Strait. It partially collapsed in 2010 and 2012 when it shed 1/3 of its floating ice in two large calving

events [*Münchow et al.*, 2014]. One of our sensors moored at 75 m below the surface was hit and damaged by a segment of an ice island in 2010.

The "normal" southern ice arch described by *Dunbar and Dunbar* [1972] formed predictably from 2003 through 2006 and again from 2010 to 2012. Furthermore, it has formed each year until 2016 (not shown). Median ice draft distributions in Nares Strait during these years are similar and, we posit, constitute the climatological mean ice conditions with a median ice thickness of about 1 m, however, more than 38% of the ice is old with drafts exceeding 2 m. Histograms of ice volume of all our data show a bimodal distribution with the primary and secondary mode in the 2.0–2.1 m and 0.1–0.3 m bins for sea ice draft, respectively. The histogram appears to decay exponentially for ice drafts exceeding 3 m. We analyzed the tails of these histograms at annual time scales to investigate the presence of a declining trend that one perhaps would expect with a diminished Arctic sea ice cover, but we find no such trend.

Multiyear sea ice with drafts exceeding 5 m constitute between 9% (2003–2004) and 16% (2007–2008) of the observed sea ice. The probability g(D) of this thick, ridged, multiyear ice decays exponentially with draft D at an e-folding scale D_0 of 3.0 ± 0.2 m. While this e-folding scale varies from year to year between 2.5 m in 2010–2011 and 3.5 m in 2009–2010, the temporal trend of D_0(t) for the 2003 to 2012 data is zero within 95% confidence. We thus conclude that thickest MY ice found in Nares Strait has not changed significantly during our observational period. We speculate that our observations document the final stage of the steady draining of the last reservoir of thick, old, MY ice that resides in the Lincoln Sea to the north of northern Ellesmere Island and Greenland. Furthermore, the sea ice distribution in Nares Strait over the last decade has become more erratic with periods of thin ice and much open water when a southern ice arch fails to form and periods of year-round southward advection of MY ice when no ice arch forms.

The apparent erratic interannual sea ice in Nares Strait perhaps suggests an ice-ocean system in transition. Hence it would be prudent to deploy in situ ice profiling sonar in Nares Strait to investigate this transition and to provide in situ observations to ground-truth both airborne (NASA Operation IceBridge) and spaceborne altimeter/radar (ICESat-2, CryoSat-2) systems. Laser and radar altimeters hold much promise to quantify ice thickness and velocity distributions in space and time with which to quantify the sea ice flux from the Arctic to the Atlantic Ocean concurrently to the west and east of Greenland.

Future work should focus on the flux of sea ice from the Arctic to the Atlantic Ocean. Unlike sea ice draft or thickness, flux implies dynamics and a metric against which to evaluate model predictions of climate physics and their changes over time. The present study constitutes a first step in this direction that allows us to tune and calibrate remote sensing studies that potentially will guide needed detail on how ice draft and velocity varies across Nares Strait and across Fram Strait. This necessary second step will provide the physical insight to facilitate dynamical prediction via a blended approach that properly accounts for both vertical and lateral ice velocity and draft variations. Such work is in progress.

Appendix A: Error Sources and Ice Draft Sensitivity

Environmental sources of error in the measurement of ice draft include nonice bodies in the path of the beam, sea surface slope, surface waves, snow load, and variations in density and sound speed (functions of salinity, temperature, and pressure in the water column). The incidence of nonice bodies in the water column is thought to be quite small. Our handling of ice drafts, on the basis of medians and probability distributions over weeks to months, is expected to insure that these occasional errors will be so small in number as to be insignificant. Sea surface slope is a very small number that is well below our precision of measurement. With regard to surface waves, the water in Nares Strait is comparatively quiescent especially when ice is on the surface. On our research cruises we saw swells on the order of 10–20 cm. There is evidence of this in the probability distributions around open water modes where one can see open water peaks straddling the 0 m point with small negative values. This error should be symmetric in distribution so that in a statistical sense, positive and negative errors would offset each other. Snow load on the ice is beyond the scope of our measurement capabilities. Average annual precipitation at nearby Pituffik during this period was 0.20 m [*Wong et al.*, 2015]. This provides an upper limit to the contribution of snow load to ice draft estimates.

The largest source of uncertainty in the calculation of ice draft, however, is attributable to the salinity and temperature characteristics of the water column, impacting the calculation of the water level, η (predominantly

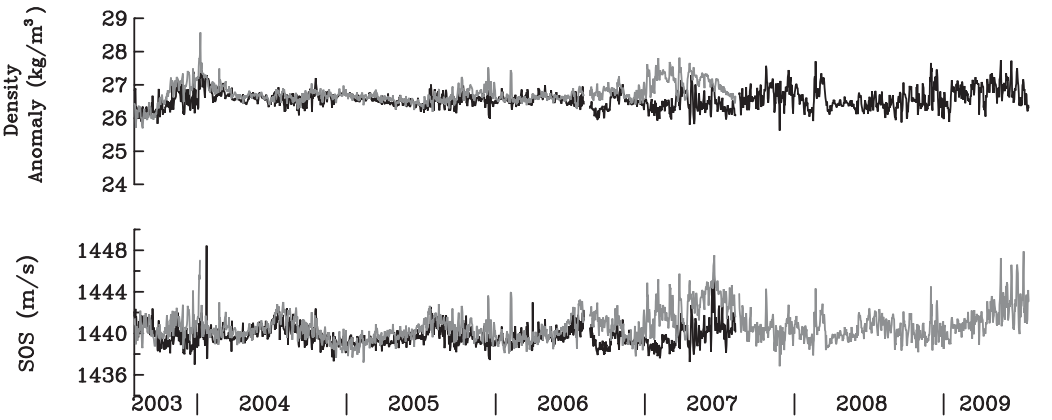

Figure A1. Water column characteristics for 2003–2009. Density and speed of sound for the upper 100 m of the water column from CT/D moorings adjacent to IPS (black: west, gray: east).

salinity), and the true speed of sound, *SS* (predominantly temperature). The partnered CT/D moorings deployed near those of the IPS are intended to provide contemporaneous measurements of these water qualities to minimize the error introduced by changes in these qualities over time. The mooring design for these instruments provides for measurements to be taken at varying depths in the water column as the tethered instruments bow down in fast currents and rise toward their nominal depth at minimal current velocities. Since measurement of salinity and temperature are instantaneous at (at most) two locations within the water column above the nominal depth of the IPS by the instruments at 30 and 80 m depths, we take advantage of the vertical sampling of the water column over a day to obtain a higher vertical resolution in salinity and temperature, and use these to extrapolate speed of sound and density integrated over the 100 and 110 m water column by the regression algorithm outlined in *Rabe et al.* [2012]. Time series of these data are shown in Figures A1 and A2.

To assess the validity of this method, we utilized a series of 10 full water column CTD casts performed adjacent to KS09 on 22 August 2007 at approximately 1 h intervals (see Figure Figure A3). Taking three randomly selected depths from each of the casts (one attainable by each of the 30, 80, and 120 m moored SBE37s), we took the salinity and temperature measured at those depths and applied the regression method to derive a speed of sound representative of the top 100 m (1441.54) and top 110 m (1441.79). Comparing these to the true values for the water column averaged over all casts, 1440.70 and 1441.00, it was found that difference in velocity would result in an error of 0.06 and 0.05 m of ice draft, respectively.

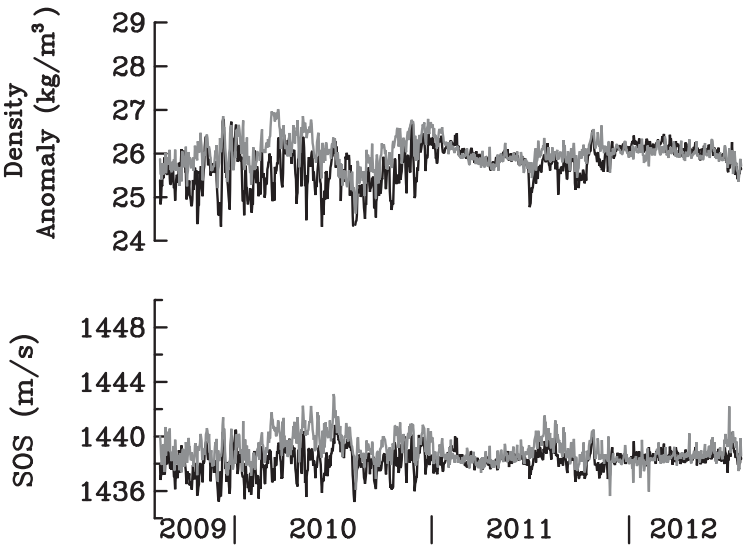

Figure A2. Water column characteristics for 2009–2012. Density and speed of sound for the upper 75 m of the water column derived from CT/D moorings adjacent to IPS (black: west, gray: east).

A daily profile for sound speed and density was then derived using the same regression method applied to the moored CT data for the 2003–2006 deployment. An analysis was performed to quantify the error introduced by the extrapolation of in situ measurements gathered at circumstantially diverse depths to represent the entire water column. It was found that the variability of daily vertical averages with the 3 year time series are $\sim$1.4 kg m^{-3} for density and $\sim$6.0 m s^{-1} for speed of sound. These give us an uncertainty of

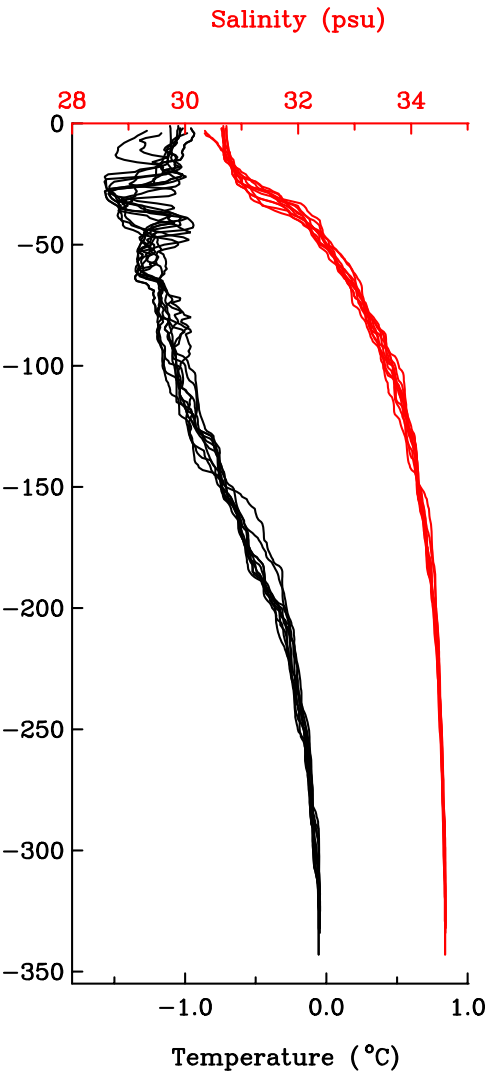

Figure A3. Salinity and temperature measurements from 10 hourly CTD casts performed adjacent to KS09 on 22 August 2007.

± 0.7 kg m^{-3} and ± 3 m s^{-1} if one assumes a vertical average that does not vary in time. The RMS misfit between data and multiple regression was found to be ~ 0.1 kg m^{-3} for density and ~ 0.4 m s^{-1} for speed of sound. We determined deviations of the magnitude of the stated uncertainty would result in an error in ice draft estimation of ~ 0.06 m for density and ~ 0.21 m for speed of sound.

The IPS rises and falls in the water column (with currents) and the water level above it rises and falls (with tides), its apex during the first deployment was at ~ 97 m depth and it often descended to ~ 106 m (on one occasion it reached a depth of ~ 112 m). With the typical range of vertical motion found to constrain the depth between 100 and 110 m, we determined that there would be a variation to the vertical average of < 0.12 kg m^{-3} for density and < 0.50 m s^{-1} for speed of sound between 100 m depth and 110 m depth. Our calculations take into account these variations in depth to first order.

Appendix B: Atmospheric Model

When model data were not available due to intermittent gaps in model output, these were generally of sufficiently short duration ($\leq$3 days) that a linear interpolation was used to span missing data. The limitation for this method was determined to be ~ 4 days by the decorrelation time scale. An alternative source for atmospheric pressure was sought for two long gaps (42 days in February/March of 2006 that are interrupted by a single day of data) as well as for the final deployment (2009–2012) during which substantial model data were unavailable. Atmospheric data measured at a NOAA meteorological station at Pituffik, Greenland (available via FTP at ftp://ftp.ncdc.noaa.gov/pub/data/gsod) were used. This site provides daily measurements of atmospheric pressure. In order to derive a relationship between measurements at Pituffik and those provided by the atmospheric model, a linear regression analysis was performed using a daily average of the model data (centered at noon) and the daily Pituffik data for a 364 day period during which both data sets were gap-free. The regression model derived was:

$$P_{\text{model}} = 82.230931 * P_{\text{Pituffik}} + 18371.4417 \quad \text{(B1)}$$

When this regression algorithm was tested against all mutually available data that had been excluded from the derivation phase, high agreement was achieved with $R^2 = 0.88$. Therefore, within the lengthy gap described above, the regression of daily Pituffik data was linearly interpolated to the frequency of the IPS range measurements.

Appendix C: Spatial Domain Derivation

Our measurements are in the time domain and we project them into the spatial domain using simultaneous velocity data. With spatial bins, each 0.1 m in length, each ice draft measurement is placed into the bin over the IPS location. All bins are assumed to move along the channel with the ice velocity. When multiple ice drafts are placed into a bin, the last one observed is used. For a given year, we then find the draft of the ice that falls into each of the bins that has traversed the location of our instruments and derive a probability

density function of ice drafts from these. Our ice year begins on 1 September and ends on 31 July. In statistical comparisons, the month of August is excluded from the data unless explicitly noted to exclude data gaps resulting from the fact that all deployment/recovery cruises occurred in that month.

Acknowledgments
The National Science Foundation supported the initial fieldwork with OPP-0230236 and analyses with OPP-1022843. The University of Delaware and the Marian R. Okie fellowship which provided substantial additional support. Instrument preparation, deployment, and recoveries were accomplished through dedicated efforts by a large group of international scientists, engineers, and technicians in addition to the captains and crews of the USCGC Healy and the CCGS Henry Larsen. Our thanks go to Humfrey Melling and David Riedel of the Canadian Department of Fisheries and Oceans who provided invaluable input and guidance related to ice data processing and to Phil Barbour of Oregon State University who provided atmospheric model data. We are also grateful to Helga Huntley who generously shared insights and suggestions. The data presented in this article can be found at https://arcticdata.io/catalog/#view/urn:uuid:47314a4d-b71e-4bb3-9449-917d7dfdac1f and https://arcticdata.io/catalog/#view/urn:uuid:6624e413-3681-4547-8c60-9418eebb069f.

References

Aagaard, K., and E. Carmack (1989), The role of sea ice and other fresh-water in the Arctic circulation, *J. Geophys. Res.*, *94*(C10), 14,485–14,498, doi:10.1029/JC094iC10p14485.

Blidberg, D., R. Corell, and A. Westneat (1981), Probable ice thickness of the Arctic Ocean, *Coastal Eng.*, *5*(2–3), 159–169, doi:10.1016/0378-3839(81)90013-2.

Bourke, R., and R. Garrett (1987), Sea ice thickness distribution in the Arctic-ocean, *Cold Reg. Sci. Technol.*, *13*(3), 259–280, doi:10.1016/0165-232X(87)90007-3.

Canadian Ice Service (2011), Sea ice climatic atlas northern Canadian waters, 1981-2010, Canadian Ice Service, Ottawa, Ontario, Canada.

Comiso, J. C., and F. Nishio (2008), Trends in the sea ice cover using enhanced and compatible AMSR-E, SSM/I, and SMMR data, *J. Geophys. Res.*, *113*, C02S07, doi:10.1029/2007JC004257.

Dumont, D., Y. Gratton, and T. E. Arbetter (2009), Modeling the dynamics of the North Water Polynya ice bridge, *J. Phys. Oceanogr.*, *39*(6), 1448–1461, doi:10.1175/2008JPO3965.1.

Dunbar, M. (1973), Ice regime and ice transport in Nares Strait, *Arctic*, *26*(4), 282–191.

Dunbar, M., and M. J. Dunbar (1972), The history of the north water, *Proc. R. Soc. Edinb. Biol.*, *72*, 231–241, doi:10.1017/S0080455X00001788.

Eicken, H., and M. Lange (1989), Sea ice thickness data: The many vs the few, *Geophys. Res. Lett.*, *16*(6), 495–498, doi:10.1029/GL016i006p00495.

Farrell, S. L., N. Kurtz, L. N. Connor, B. C. Elder, C. Leuschen, T. Markus, D. C. McAdoo, B. Panzer, J. Richter-Menge, and J. G. Sonntag (2012), A first assessment of Ice Bridge snow and ice thickness data over Arctic sea ice, *IEEE Trans. Geosci. Remote Sens.*, *50*(6), 2098–2111, doi:10.1109/TGRS.2011.2170843.

Haas, C., S. Hendricks, and M. Doble (2006), Comparison of the sea-ice thickness distribution in the Lincoln Sea and adjacent Arctic Ocean in 2004 and 2005, *Ann. Glaciol.*, *44*, 247–252 doi:10.3189/172756406781811781.

Hansen, E., S. Gerland, M. A. Granskog, O. Pavlova, A. H. H. Renner, J. Haapala, T. B. Loyning, and M. Tschudi (2013), Thinning of Arctic sea ice observed in Fram Strait: 1990-2011, *J. Geophys. Res. Oceans*, *118*, 5202–5221, doi:10.1002/jgrc.20393.

Hibler, W. (1979), Dynamic thermodynamic sea ice model, *J. Phys. Oceanogr.*, *9*(4), 815–846, doi:10.1175/1520-0485(1979)009<0815:ADTSIM>2.0.CO;2.

Johnston, M. E. (2014), A decade of probing the depths of thick multi-year ice to measure its borehole strength, *Cold Reg. Sci. Technol.*, *99*, 46–65, doi:10.1016/j.coldregions.2013.12.002.

Kay, J. E., M. M. Holland, and A. Jahn (2011), Inter-annual to multi-decadal Arctic sea ice extent trends in a warming world, *Geophys. Res. Lett.*, *38*, L15708, doi:10.1029/2011GL048008.

Kurtz, N. T., S. L. Farrell, M. Studinger, N. Galin, J. P. Harbeck, R. Lindsay, V. D. Onana, B. Panzer, and J. G. Sonntag (2013), Sea ice thickness, freeboard, and snow depth products from Operation Ice Bridge airborne data, *Cryosphere*, *7*(4), 1035–1056.

Kwok, R. (2005), Variability of Nares Strait ice flux, *Geophys. Res. Lett.*, *32*, L24502, doi:10.1029/2005GL024768.

Kwok, R. (2015), Sea ice convergence along the Arctic coasts of Greenland and the Canadian Arctic Archipelago: Variability and extremes (1992–2014), *Geophys. Res. Lett.*, *42*, 7598–7605, doi:10.1002/2015GL065462.

Kwok, R., and G. F. Cunningham (2010), Contribution of melt in the Beaufort Sea to the decline in Arctic multiyear sea ice coverage: 1993–2009, *Geophys. Res. Lett.*, *37*, L20501, doi:10.1029/2010GL044678.

Kwok, R., and G. F. Cunningham (2016), Contributions of growth and deformation to monthly variability in sea ice thickness north of the coasts of Greenland and the Canadian Arctic Archipelago, *Geophys. Res. Lett.*, *43*, 8097–8105, doi:10.1002/2016GL069333.

Kwok, R., G. F. Cunningham, M. Wensnahan, I. Rigor, H. J. Zwally, and D. Yi (2009), Thinning and volume loss of the Arctic Ocean sea ice cover: 2003–2008, *J. Geophys. Res.*, *114*, C07005, doi:10.1029/2009JC005312.

Kwok, R., L. T. Pedersen, P. Gudmandsen, and S. S. Pang (2010), Large sea ice outflow into the Nares Strait in 2007, *Geophys. Res. Lett.*, *37*, L03502, doi:10.1029/2009GL041872.

Laxon, S. W., et al. (2013), CryoSat-2 estimates of Arctic sea ice thickness and volume, *Geophys. Res. Lett.*, *40*, 732–737, doi:10.1002/grl.50193.

Maslanik, J. A., C. Fowler, J. Stroeve, S. Drobot, J. Zwally, D. Yi, and W. Emery (2007), A younger, thinner Arctic ice cover: Increased potential for rapid, extensive sea-ice loss, *Geophys. Res. Lett.*, *34*, L24501, doi:10.1029/2007GL032043.

Maslanik, J., J. Stroeve, C. Fowler, and W. Emery (2011), Distribution and trends in Arctic sea ice age through spring 2011, *Geophys. Res. Lett.*, *38*, L13502, doi:10.1029/2011GL047735.

Maykut, G., and N. Untersteiner (1971), Some results from a time-dependent thermodynamic model of sea ice, *J. Geophys. Res.*, *76*(6), 1550–1575, doi:10.1029/JC076i006p01550.

Meehl, G. A., et al. (2012), Climate system response to external forcings and climate change projections in CCSM4, *J. Clim.*, *25*(11), 3661–3683, doi:10.1175/JCLI-D-11-00240.1.

Melling, H., and D. Riedel (1995), The underside topography of sea-ice over the continental-shelf of the Beaufort Sea in the winter of 1990, *J. Geophys. Res.*, *100*(C7), 13,641–13,653, doi:10.1029/95JC00309.

Melling, H., P. Johnston, and D. Riedel (1995), Measurements of the underside topography of sea-ice by moored subsea sonar, *J. Atmos. Oceanic Technol.*, *12*(3), 589–602, doi:10.1175/1520-0426(1995)012.

Melling, H., Y. Gratton, and G. Ingram (2001), Ocean circulation within the North Water Polynya of Baffin Bay, *Atmos. Ocean*, *39*(3), 301–325, doi:10.1175/1520-0426(1995)012.

Münchow, A. (2016), Volume and freshwater flux observations from Nares Strait to the West of Greenland at daily time scales from 2003 to 2009, *J. Phys. Oceanogr.*, *46*(1), 141–157, doi:10.1175/JPO-D-15-0093.1.

Münchow, A., and H. Melling (2008), Ocean current observations from Nares Strait to the west of Greenland: Interannual to tidal variability and forcing, *J. Mar. Res.*, *66*(6), 801–833.

Münchow, A., L. Padman, and H. A. Fricker (2014), Interannual changes of the floating ice shelf of Petermann Gletscher, North Greenland, from 2000 to 2012, *J. Glaciol.*, *60*(221), 489–499, doi:10.3189/2014JoG13J135.

Perovich, D., J. Richter-Menge, C. Polashenski, B. Elder, T. Arbetter, and O. Brennick (2014), Sea ice mass balance observations from the North Pole environmental observatory, *Geophys. Res. Lett.*, *41*, 2019–2025, doi:10.1002/2014GL059356.

Preußer, A., G. Heinemann, S. Willmes, and S. Paul (2015), Multi-decadal variability of polynya characteristics and ice production in the north water polynya by means of passive microwave and thermal infrared satellite imagery, *Remote Sens.*, *7*(12), 15,844–15,867, doi: 10.3390/rs71215807.

Rabe, B., A. Münchow, H. L. Johnson, and H. Melling (2010), Nares Strait hydrography and salinity field from a 3-year moored array, *J. Geophys. Res.*, *115*, C07010, doi:10.1029/2009JC005966.

Rabe, B., H. L. Johnson, A. Münchow, and H. Melling (2012), Geostrophic ocean currents and freshwater fluxes across the Canadian polar shelf via Nares Strait, *J. Mar. Res.*, *70*(4), 603–640.

Renner, A. H. H., S. Gerland, C. Haas, G. Spreen, J. F. Beckers, E. Hansen, M. Nicolaus, and H. Goodwin (2014), Evidence of Arctic sea ice thinning from direct observations, *Geophys. Res. Lett.*, *41*, 5029–5036, doi:10.1002/2014GL060369.

Samelson, R. M., and P. L. Barbour (2008), Low-level jets, orographic effects, and extreme events in Nares Strait: A model-based mesoscale climatology, *Mon. Weather Rev.*, *136*(12), 4746–4759, doi:10.1175/2007MWR2326.1.

Samelson, R., T. Agnew, H. Melling, and A. Munchow (2006), Evidence for atmospheric control of sea-ice motion through Nares Strait, *Geophys. Res. Lett.*, *33*, L02506, doi:10.1029/2005GL025016.

Schledermann, P. (1980), Notes on Norse finds from the east coast of Ellesmere Island, NWT, *Arctic*, *33*(3), 454–463.

Shibata, H., K. Izumiyama, K. Tateyama, H. Enomoto, and S. Takahashi (2013), Sea-ice coverage variability on the Northern Sea Routes, 1980-2011, *Ann. Glaciol.*, *54*(62), 139–148, doi:10.3189/2013AoG62A123.

Shroyer, E. L., L. Padman, R. Samelson, A. Münchow, and L. Stearns (2017), Seasonal control of Petermann Gletscher ice-shelf melt by the ocean's response to sea-ice cover in Nares Strait, *J. Glaciol.*, *63*(238), 324–330, doi:10.1029/2011GL047735.

Smith, S., R. Muench, and C. Pease (1990), Polynyas and leads: An overview of physical processes and environment, *J. Geophys. Res.*, *95*(C6), 9461–9479, doi:10.1029/JC095iC06p09461.

Stroeve, J., M. Serreze, S. Drobot, S. Gearheard, M. Holland, J. Maslanik, W. Meier, and T. Scambos (2008), Arctic sea ice extent plummets in 2007, *EOS Trans. AGU*, *89*(2), 13.

Stroeve, J. C., V. Kattsov, A. Barrett, M. Serreze, T. Pavlova, M. Holland, and W. N. Meier (2012), Trends in Arctic sea ice extent from CMIP5, CMIP3 and observations, *Geophys. Res. Lett.*, *39*, L16502, doi:10.1029/2012GL052676.

Thorndike, A. (2000), Sea ice thickness as a stochastic process, *J. Geophys. Res.*, *105*(C1), 1311–1313, doi:10.1029/1999JC900271.

Thorndike, A., D. Rothrock, G. Maykut, and R. Colony (1975), Thickness distribution of sea ice, *J. Geophys. Res.*, *80*(33), 4501–4513, doi: 10.1029/JC080i033p04501.

Vavrus, S. J., M. M. Holland, A. Jahn, D. A. Bailey, and B. A. Blazey (2012), Twenty-first-century arctic climate change in CCSM4, *J. Clim.*, *25*(8), 2696–2710, doi:10.1175/JCLI-D-11-00220.1.

Vincent, R. F., R. F. Marsden, P. J. Minnett, and J. R. Buckley (2008), Arctic waters and marginal ice zones: 2. An investigation of arctic atmospheric infrared absorption for advanced very high resolution radiometer sea surface temperature estimates, *J. Geophys. Res.*, *113*, C08044, doi:10.1029/2007JC004354.

Wadhams, P. (1981), Sea-ice topography of the Arctic Ocean in the region 70-degrees-w to 25-degrees-e, *Philos. Trans. R. Soc. A*, *302*(1464), 45–85, doi:10.1098/rsta.1981.0157.

Wadhams, P., A. Gill, and P. Linden (1979), Transects by submarine of the east Greenland and polar front, *Deep Sea Res., Part A*, *26*(12), 1311–1327, doi:10.1016/0198-0149(79)90001-3.

Wong, G. J., E. C. Osterberg, R. L. Hawley, Z. R. Courville, D. G. Ferris, and J. A. Howley (2015), Coast-to-interior gradient in recent northwest Greenland precipitation trends (1952-2012), *Environ. Res. Lett.*, *10*(11), 1–12, doi:10.1088/1748-9326/10/11/114008.